Univerzita Palackého v Olomouci
Přírodovědecká fakulta
Katedra experimentální fyziky

DIPLOMOVÁ PRÁCE

Modelování optické části detektoru času průletu vysokoenergetických částic a srovnání s daty

Vypracoval	**Tomáš Komárek**
Studijní program	N1701 Fyzika
Studijní obor	Aplikovaná fyzika
Forma studia	Prezenční
Vedoucí diplomové práce	Mgr. Libor Nožka, Ph.D.
Termín odevzdání práce	Srpen 2016

Palacký University Olomouc
Faculty of Science
Department of Experimental Physics

DIPLOMA THESIS

Simulation of optical part of high-energy particle time-of-flight detector and comparison with data

Author	**Tomáš Komárek**
Study programme	N1701 Physics
Field of study	Applied Physics
Study form	Full time
Supervisor	Mgr. Libor Nožka, Ph.D.
Submission date	August 2016

Bibliografická identifikace

Jméno a příjmení autora	Tomáš Komárek
Název práce	Modelování optické části detektoru času průletu vysokoenergetických částic a srovnání s daty
Typ práce	Diplomová
Pracoviště	Katedra experimentální fyziky
Vedoucí práce	Mgr. Libor Nožka, Ph.D.
Rok obhajoby práce	2016
Abstrakt	Detektor AFP je navržen k pokrytí dosud nepokrytého kinematického rozsahu v dopředné oblasti detektoru ATLAS. Při měřeních s vysokou luminozitou však nastává problém s pile-upem, kdy detektor potřebuje rozeznat, ze kterého vertexu každá zachycená částice pochází. Toho lze dosáhnout měřením času příletu. Pro tento účel byl navržen detektor času letu, jehož prototyp je studován jak pomocí simulace, tak analýzou dat získaných při testovacích měřeních pomocí svazku urychlovače. Důraz je kladen na analýzu korelací mezi jednotlivými měřeními, které tento detektor provádí. Tato měření je cílem průměrovat a tím vylepšit výsledné rozlišení, přílišné korelace by však tento efekt kazily. Výsledky simulací a analýzy reálných dat jsou poté srovnány a jsou učiněny závěry ohledně očekávaného výkonu a chování detektoru.
Klíčová slova	Částicová fyzika, dopředný detektor, detektor času letu, CERN, LHC, ATLAS, AFP
Počet stran	56
Počet příloh	1
Jazyk	Anglický

Bibliographical identification

Autor's first name and surname	Tomáš Komárek
Title	Simulation of optical part of high-energy particle time-of-flight detector and comparison with data
Type of thesis	Master
Department	Department of Experimental Physics
Supervisor	Mgr. Libor Nožka, Ph.D.
The year of presentation	2016
Abstract	The AFP detector is designed to cover a new kinematic region in the ATLAS forward region. However, during a high luminosity runs, the detector needs a means of distinguishing from which vertex the particles originate. This can be achieved by measuring the time of arrival of these particles. A ToF (Time of Flight) detector prototype designed for this purpose is studied, both by Monte Carlo simulations and by analysis of data acquired during a Test Beam. The focus is on possible correlations between the individual measurements the detector performs, which are then to be averaged, improving the timing resolution. Excessive correlation can destroy this effect. The results of the simulation and the real data analysis are then compared and conclusions drawn regarding the expected detector performance.
Keywords	Particle physics, forward detector, Time-of-Flight detector, CERN, LHC, ATLAS, AFP
Number of pages	56
Number of appendices	1
Language	English

Prohlášení

Prohlašuji, že jsem předloženou diplomovou práci vypracoval samostatně pod vedením Mgr. Libora Nožky, Ph.D. a že jsem použil zdrojů, které cituji a uvádím v seznamu použitých pramenů.

V Olomouci dne 14. srpna 2016

.....

Tomáš Komárek

Poděkování

Chtěl bych tímto poděkovat svým rodičům za dlouhodobou podporu, všem členům skupiny částicové fyziky na SLO UP Olomouc za četné konzultace okolností měření i průběžných výsledků, především pak vedoucímu práce Mgr. Liboru Nožkovi, Ph.D. za veškerou pomoc s interpretací výsledků a finální kontrolu práce.

Contents

Introduction

This diploma thesis covers the design and construction of a new time-of-flight (ToF) detector to be used in high energy physics. The main emphasis is on a simulation of the optical part of the detector and the comparison of these simulations with the real data acquired at the September 2015 AFP Test Beam measurements. For most of the analysis, the ROOT framework[1] will be used.

Motivation for time-of-flight detector construction

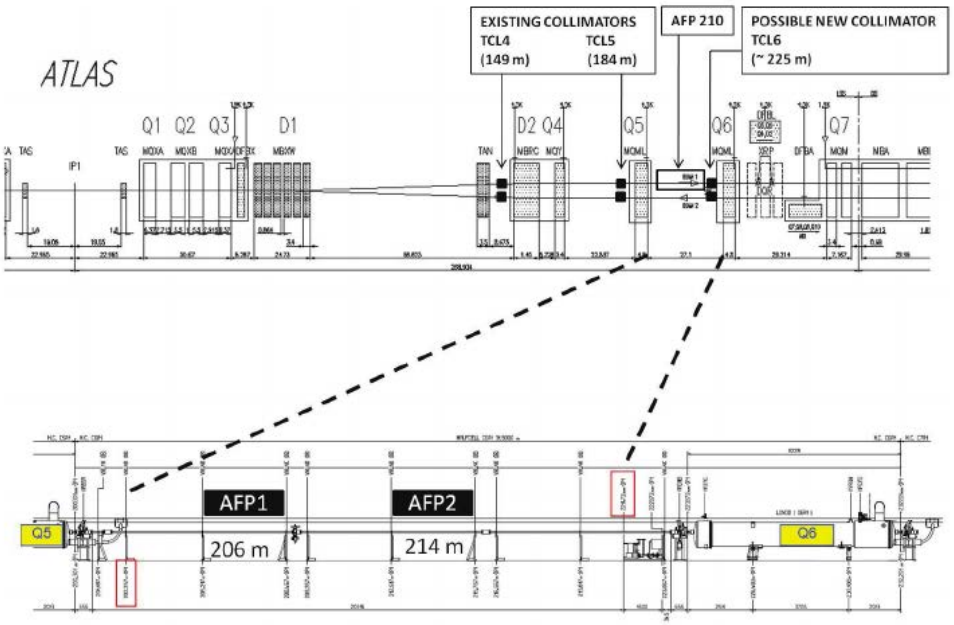

Figure 1: Scheme of the AFP stations placement. Credit: [1].

Our effort to construct a time-of-flight detector is motivated by the needs of the new AFP (ATLAS Forward Proton) detector [1], which is currently being developed for use in the ATLAS forward region. The AFP detector is designed to detect protons that went through inelastic scattering and therefore lost some of their original energy. This will allow to have a complete information about some scattering processes, where only the products in the ATLAS central detector were previously available. Some scattering processes can be measured with the already present ALFA detector, like the exclusive pion production $pp \to pp\,\pi^+\pi^-$ [2], but the main focus of the ALFA detector is on elastic events and the kinematic area covered is not sufficient for many processes where

[1] See `https://root.cern.ch/`.

the energy the protons lose is higher. More details on processes constituting the main AFP physics programme can be found in [1].

An important thing to consider regarding the placement of the AFP stations is that there are several LHC magnets (dipoles and quadrupoles) between their positions and the IP. Due to their energy loss, the trajectory of the surviving protons is influenced more by the magnets of the LHC and they diverge from the beam [3]. The AFP detector is therefore placed on both outgoing sides in the forward region very close to the beam, where it can cover kinematic area that is of interest. The placement of the AFP stations on one of the sides is described by Figure 1.

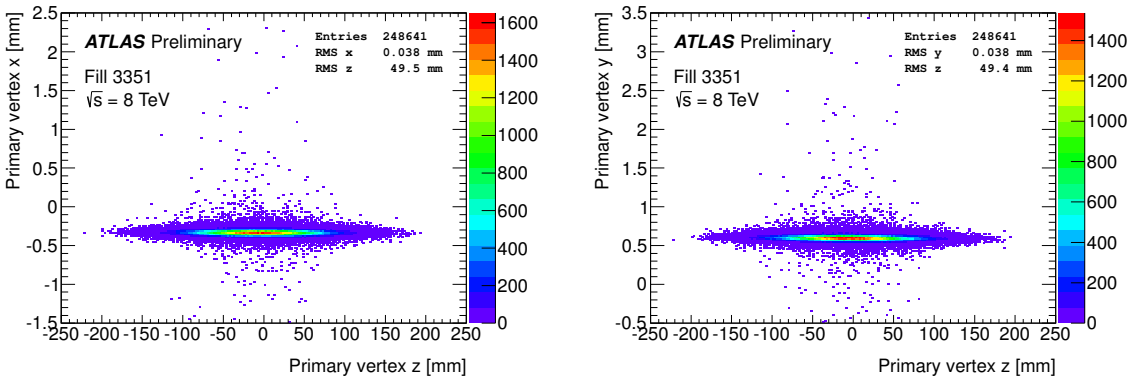

Figure 2: Vertex x-z and y-z distributions in the ATLAS detector during the LHC fill 3351. The prolonged beam spot shape along the z axis (aligned with the beamline) is clearly visible. Credit: [4].

The ToF detector is needed due to the pileup in high luminosity LHC runs for which the AFP detector was designed. When there are multiple collisions within one bunch crossing (in-time pileup), there is a possibility that protons from two unrelated collisions detected by the AFP would imitate products of a single collision. Out-of-time pileup (collisions from subsequent bunch crossings) could be in some situations discerned by the AFP tracker time resolution alone, but the ToF detector helps with these too. Still, the in-time pileup is of the main concern. The beam spot[2] is very small in the transverse plane, but quite long ($\sim 40 - 50\,\mathrm{mm}$) along the beam axis [5]. The beam spot shape is shown in Figure 2, an example of a pileup situation can be seen in Figure 3.

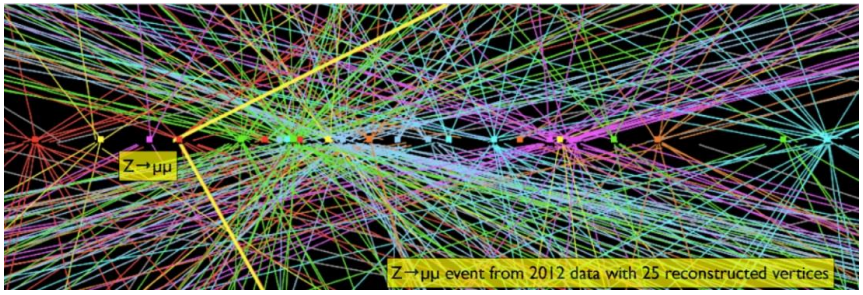

Figure 3: An example of the in-time pileup with 25 reconstructed vertices. The figure shows area $\sim 6\,\mathrm{cm}$ across. Credit: ATLAS Collaboration.

[2]The area, where collisions occur.

The vertex position in the transverse plane from which given proton is coming cannot be determined due to a very long lever arm with respect to the AFP tracker. It is therefore useful to know the position of the vertex from which the proton originated along the beam axis. It is possible to determine this by measuring the time at which the protons arrive to the AFP stations, as all protons travel very close to the speed of light. However, this approach requires very high timing precision. The target precision of the ToF detector in question is 10 ps, which translates to ~ 1.5 mm of spatial resolution. This information about the collision vertex position can then be matched with an appropriate vertex detected by the ATLAS central detector.

Chapter 1

The theory of Cherenkov radiation and light propagation in a medium

The Cherenkov radiation is a pivotal phenomenon for the ToF detector. It is the source of the optical signal, which is used for the precise timing measurements carried out by the detector.

1.1 The origin of Cherenkov radiation

The Cherenkov radiation is emitted by highly relativistic particles which enter a medium, where the speed of light is smaller than the speed of the particle itself. In homogeneous isotropic materials, photons are emitted at any given point in a cone facing forward, symmetry axis of the cone is equivalent to the particle direction. The angle of the cone as well as the distribution of the Cherenkov radiation wavelengths are determined by the particle speed and the refractive index of the medium for given photon wavelength. As the particle passes through the medium, a shockwave-like expanding cone of photons is created behind it.

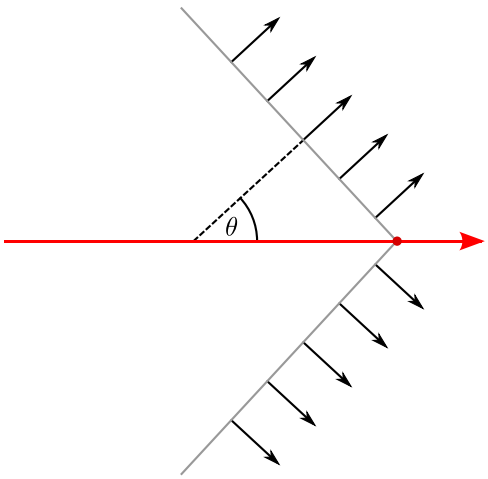

Figure 1.1: A Cherenkov radiation cone created by a passing particle (red).

When the condition $c/n < v_{\mathrm{p}} < c$ is met, the Cherenkov radiation as illustrated in Figure 1.1 is emitted in a cone with the angle θ given by Equation 1.1, where v_{p} is the speed of the particle, n is the index of refraction for given photon wavelength and c is the speed of light in vacuum [6]:

$$\cos\theta = \frac{c}{nv_\mathrm{p}}\,. \tag{1.1}$$

However, to determine the angle θ, we need to know the wavelength of the photon first. The relation describing energy emitted per length the particle travelled through the medium at given frequency ω can be derived from the Frank–Tamm formula as shown in Equation 1.2, where μ is the permeability of the medium:

$$\frac{\mathrm{d}E}{\mathrm{d}x} = \frac{q^2}{4\pi}\int_{v_\mathrm{p}>\frac{c}{n(\omega)}} \mu(\omega)\omega\left(1 - \frac{c^2}{v_p^2 n^2(\omega)}\right)\mathrm{d}\omega\,. \tag{1.2}$$

Based on Equation 1.2 we can see that higher frequencies, hence shorter wavelengths, are more pronounced. It turns out most of the Cherenkov radiation is in the ultraviolet spectrum. But only those wavelengths are emitted for which the velocity in the medium is less than that of the particle.

The Cherenkov radiation is by nature highly linearly polarized. The polarization vector depends on the position on the Cherenkov cone and always lies in the plane defined by the particle and photon propagation directions [7]. Therefore the polarization vector for photons in Figure 1.1 is parallel to the gray line depicting the expanding cone of photons.

1.2 Cherenkov light propagation in a medium via internal reflection

The total reflection is a crucial mechanism for the light propagation within the ToF optical part, as will be described further in section 2.4. The critical angle φ_c for total reflection can be derived from the Snell's law (Equation 1.3) by fixing the angle of transmission φ_t to 90° and finding the corresponding angle of incidence $\varphi_\mathrm{i} = \varphi_\mathrm{c}$:

$$n_1 \sin\varphi_\mathrm{i} = n_2 \sin\varphi_\mathrm{t}\,, \tag{1.3}$$

$$\varphi_\mathrm{c} = \arcsin\frac{n_2}{n_1}\,. \tag{1.4}$$

For any angle of incidence $\varphi_\mathrm{i} \geq \varphi_\mathrm{c}$, where the critical angle φ_c is given by Equation 1.4, total internal reflection will occur. It is obvious that total reflection can occur only when the photon is travelling through a medium with index of refraction n_1 larger than the index of refraction n_2 corresponding to the medium beyond the boundary.

However, some photons don't reach the critical angle for the total reflection and then propagate through imperfect internal reflections or leave the medium. The reflection/transmission ratio for this reflection mechanism heavily depends on the polarization of the photons, as is described by Fresnel equations. By incorporating the Snell's law, those can be simplified [8], giving Equation 1.5 for the reflectivity of the p-polarized photons (parallel to the plane of incidence) and Equation 1.6 for reflectivity of the s-polarized photons (perpendicular to the plane of incidence).

$$r_\mathrm{p} = -\frac{\tan(\varphi_\mathrm{i} - \varphi_\mathrm{t})}{\tan(\varphi_\mathrm{i} + \varphi_\mathrm{t})}\,, \tag{1.5}$$

$$r_\mathrm{s} = -\frac{\sin(\varphi_\mathrm{i} - \varphi_\mathrm{t})}{\sin(\varphi_\mathrm{i} + \varphi_\mathrm{t})}\,. \tag{1.6}$$

Chapter 2

Description of the ToF detector

While the ToF detector is developed for the AFP project, it is designed to be a standalone detector with many possible use-cases. However, the integration with the AFP tracker will be briefly discussed.

2.1 The AFP Roman Pots

The position of the AFP detector stations can be seen in Figure 1, see Introduction. The AFP detector uses the so-called Roman Pot (RP) containers to store the detection hardware. This poses serious spatial constraints, as the detector has to fit into the cylindric space available. A previous proposal to use an alternative approach with the so-called Hamburg beampipe, which would provide considerably more space, was rejected.

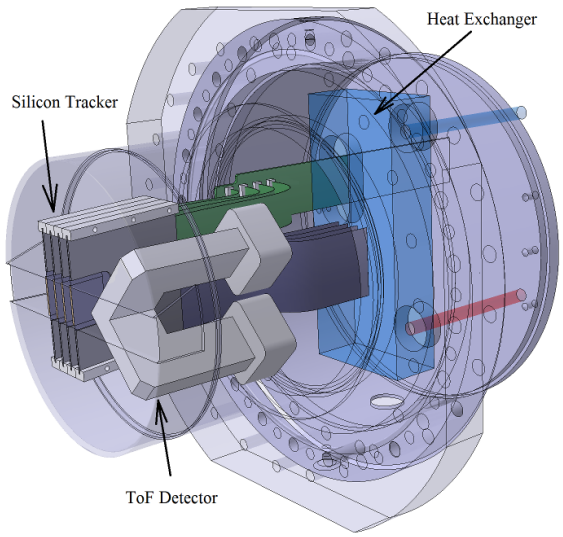

Figure 2.1: The AFP Roman Pot. Credit: [1].

There are two AFP Roman Pots on each side of the ATLAS IP, however only one of them on each side is fitted with a ToF detector. The ToF detector is always in the RP further from the IP. This is due to particle showers that could be caused by the

added material, which would influence the performance of the tracker in the other pot. On the contrary, the silicon tracker is present in all AFP stations. An AFP Roman Pot scheme with both the tracker and the ToF detector installed is shown in Figure 2.1.

2.2 The AFP tracker

The AFP tracker comprises of four layers of 3D silicon pixel tracker FE-I4 modules [1]. Each module has pixel dimensions of 50 μm in the horizontal and 250 μm in the vertical direction. In order to improve horizontal resolution as well as the hit efficiency, the modules are installed with a slight tilt of 14° around the vertical axis. The resolution in the vertical plane is improved by $\sim 60\,\mu$m staggering of the modules.

2.3 Overview of the ToF detector

As was mentioned earlier, the ToF detector is just one part of the AFP project, but it can also act as a standalone detector. The chain of the ToF signal gathering and processing apparatus is discussed in this section.

A block scheme of the ToF detector main parts is in Figure 2.2. The optical part consists of fused silica bars, where the Cherenkov radiation is generated by passing particles, and a photomultiplier (MCP-PMT). The response of the photomultiplier is then amplified by two stages of pre-amplifiers and processed by the constant fraction discriminator (CFD), to be fed to the clock (HPTDC) to determine the time with high precision. This digital information is then used by the data acquisition system (RCE). More detailed description of the individual parts follows.

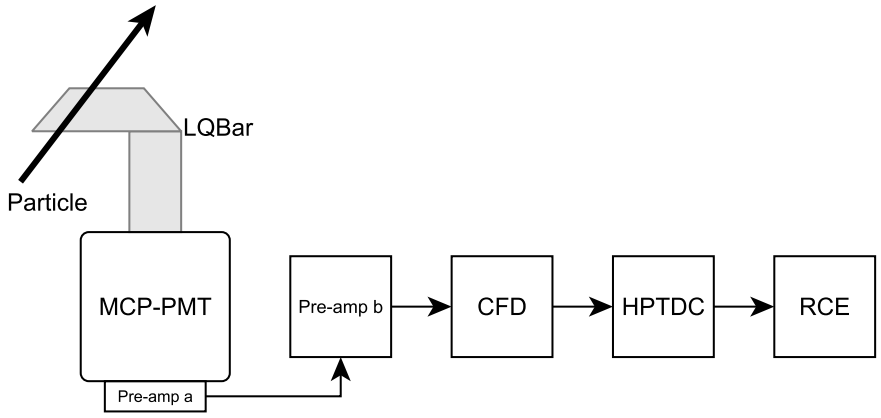

Figure 2.2: ToF detector block scheme.

Optical part

The optical part of the ToF detector is made of the fused silica material, where the Cherenkov radiation is generated by passing particles and guided towards the photomultiplier. The photomultiplier used is the miniPLANACON XPM85112 MCP-PMT (multi-channel plate photomultiplier) with 10 μm pore size, manufactured by Photonis [9]. More in-depth description of the optical part follows in section 2.4.

Amplifiers

There are two pre-amplifier stages, denoted PAa and PAb. The first pre-amplifier also acts as a current to voltage converter, being connected directly to the back of the MCP-PMT to minimize losses and potential noise. Each stage has a 20 dB gain (10× gain in voltage). The output saturation level is about 2.5 V for PAa and 2 V for PAb, therefore only PAb saturation has to be taken into account. The PMT high voltage has to be set accordingly in order to prevent saturation, which would affect the CFD timing performance.

Constant fraction discriminator

The CFD (Constant fraction discriminator) board is a crucial element for a precision timing. It splits the amplified PMT signal and compares an attenuated version to a delayed version of the same original input signal. Whenever these two intersect, that is the trigger point, as described by Figure 2.3. This technique significantly reduces influence of the input signal amplitude on the trigger point, provided the signal shape does not vary.

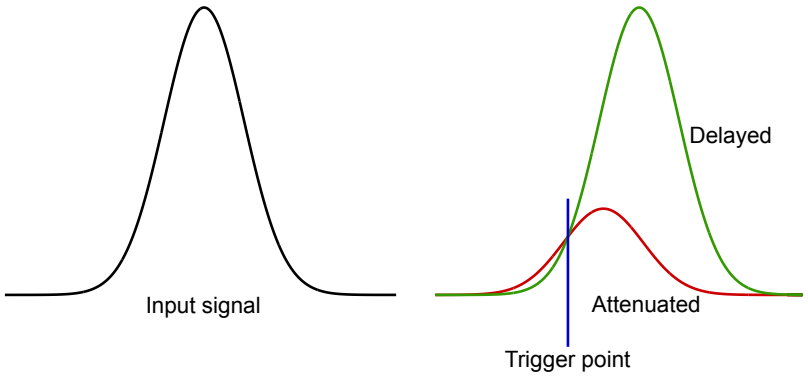

Figure 2.3: CFD triggering mechanism.

HPTDC

HPTDC stands for High-Performance Time-to-Digital Converter. It is the means of converting the CFD trigger signal to a precise timing information. It operates by running a 25 ns loop of 1024 clock ticks, yielding a 24.4 ps resolution per tick. The output is the information about which tick coincided with the trigger signal.

An improved new version of the HPTDC board with 3 ps resolution may be available in the near future, further enhancing the overall detector timing performance.

RCE

RCE is the Reconfigurable Cluster Elements system. It is employed as the data acquisition system for the AFP detector, storing data in the ROOT data format. More information regarding the RCE system can be found in [10].

2.4 Optical part of the ToF detector

The optical part of the ToF detector consists of 16 fused silica bars in a 4×4 pattern, reflecting the layout of the channels on the MCP-PMT. Their assembly can be seen in Figure 2.4. The bars are meant to generate a Cherenkov radiation signal when a particle passes through and guide it to the photomultiplier channels. While 60 % of the signal is generated by photons travelling directly, total reflection within the bars is crucial to ensure that strong enough signal reaches the photomultiplier. The imperfect internal reflection may also play some minor role, as discussed in section 1.2.

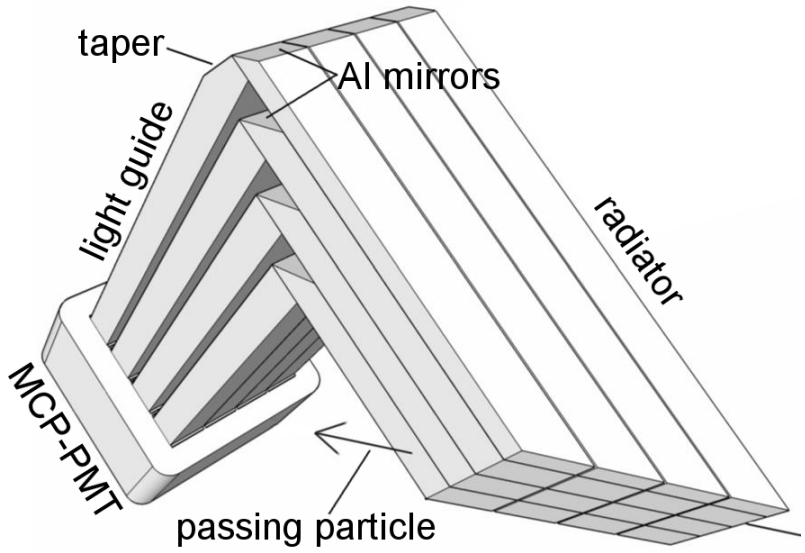

Figure 2.4: ToF detector optical part scheme. The arrow marks a particle which generates the Cherenkov radiation.

Due to the spatial constraints imposed by the Roman Pot, the bars are glued together from two parts in a 90° angle to form an L shape, called the LQBar [11]. The part of the bars that is meant to emit the Cherenkov radiation is called the radiator, the other part leading to the MCP-PMT is called the light guide. The radiator is angled at the Cherenkov angle of 48° with respect to the expected particle direction. This means that a part of the optical signal travels through the LQBar in a direct way with minimal number of reflections. In the joint, there is a surface with aluminium coating, forming a mirror angled at 45°. This mirror is present in order to reflect Cherenkov photons that could escape by not fulfilling the total reflection criteria on that surface. However, the reflective capabilities of this mirror ($\sim 90\%$) are considerably worse than that of the total reflection process. Another limiting factor is the glue (Epotek 305) holding the bar parts together, as it's spectral transmittance cuts off some shorter wavelengths, which would otherwise be a useful signal. This could be mitigated by using the optical contact bonding method, which will be evaluated in the near future.

The row of bars in the direction of the detected particle is called a train. In the ideal case, when a particle passes through the detector, all bars in a single train are hit and produce a signal. Thanks to the 48° angle of the radiator part, the Cherenkov photons at the most common wavelengths $200-400\,\mathrm{nm}$ [11] reach the PMT at the same time in all bars. This enables us to use these as separate measurements. Signal from each bar is processed separately (by the described electronics chain), which allows for better resolution provided the signals from bars in a train are not correlated, or only

slightly. An analysis of this potential correlation is one of the major topics covered. The less crosstalk induced correlation between the bars in a train, the closer will the overall performance get to the theoretical resolution improvement by the factor $\frac{1}{\sqrt{n}}$ for n uncorrelated bars. Therefore if no correlation is present at all with four bars per train, we would obtain double the resolution compared to a single bar.

The first train (one closest to the beam) is modified by adding a taper behind the mirror. This means the radiator is thinner, which is useful, because this area will be exposed to more radiation than the bars further from the beam. The taper also helps to collect more optical signal, which would otherwise escape the bar. More insight on the effects of the taper is given in section 3.3, where results of the simulation are discussed. In the future, the taper might be used on more trains than just the first one.

2.5 The Test Beam setup

The setup used for the Test Beam measurements differed from the above AFP and ToF design. Only a preliminary prototype was used, also the orientation in the plane transverse to the beam differed. While for the final Roman Pot installation the radiator part will be vertical with the PMT to the side (Figure 2.1), here it was horizontal with the PMT below for easy installation and manipulation with the bars.

Description of the measuring equipment layout

In the Test Beam measurements to be evaluated, only two bars per train are present. This still allows for an evaluation of the crosstalk between the bars in a train, with the added advantage that the missing bars will not influence the two bars by their potential crosstalk, allowing for easier analysis of the actual magnitude of the crosstalk between the bars. However, the final detector resolution cannot be determined with this setup. Some estimate could be extrapolated from the resolution measured this way, but it is expected that the bars further from each other would suffer much less crosstalk and correlation than neighbouring ones. This expectation is also put under test based on the results of the measurements, where there was a gap between the bars caused by leaving one empty PMT channel between them.

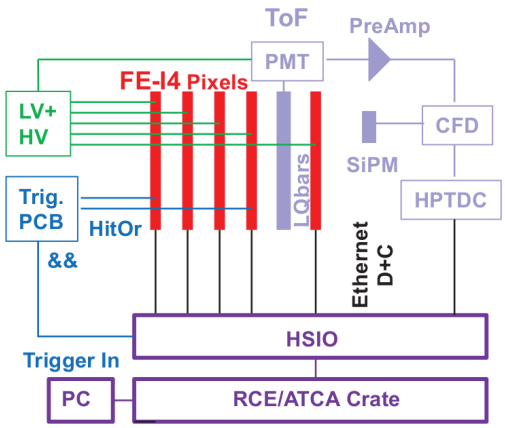

Figure 2.5: The testbeam setup block scheme. Credit: [12].

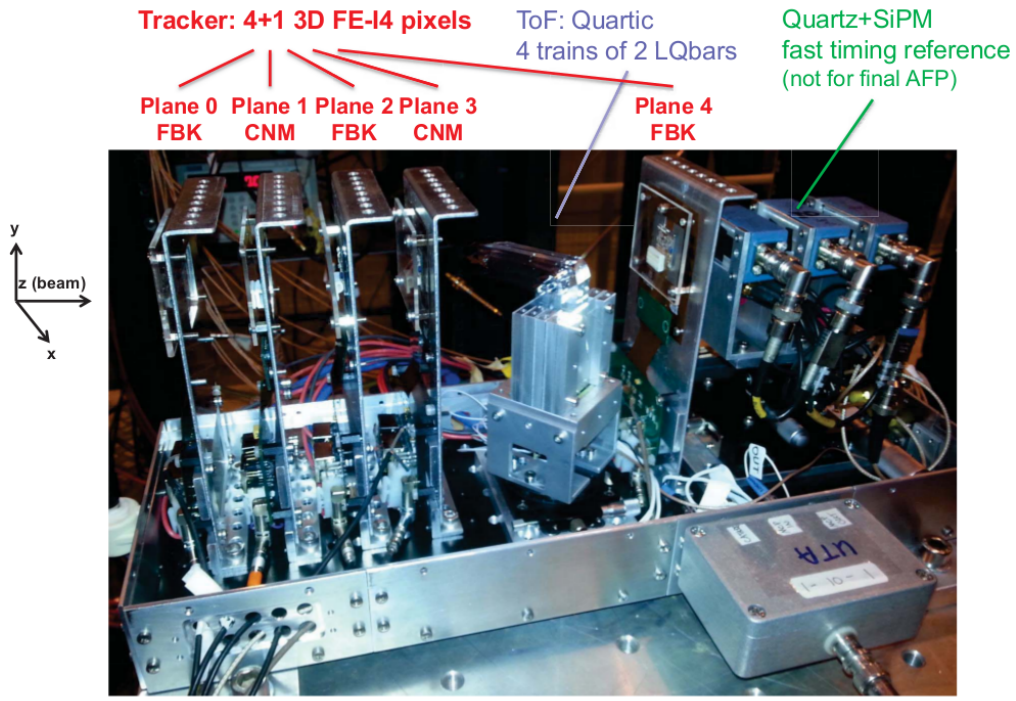

Figure 2.6: The Test Beam setup. Credit: [12].

The basic Test Beam setup is described by Figure 2.5, the physical layout can be seen in Figure 2.6 together with the coordinate system used. After four AFP tracker plates, there is the ToF detector, followed by another tracker plate and a SiPM (silicon photomultiplier, an avalanche photodiode). The SiPM acted as a trigger, picking only those pions that passed through a 3 cm long fused silica bar in front of the SiPM, covering a square area of 3×3 mm in the transverse plane. The triggering SiPM detected Cherenkov radiation from the bar, producing a strong signal due to the bar length enabling more radiation to hit the detector. The advantage of this trigger is that we can choose the measured area according to our needs, for example to analyse behaviour when different parts of the bar are hit.

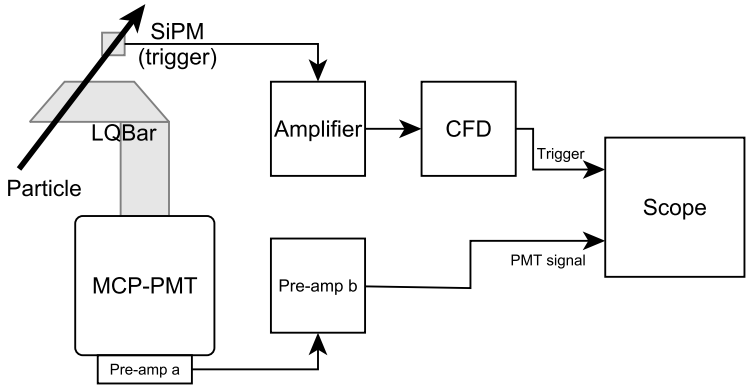

Figure 2.7: The oscilloscope measurements setup block scheme.

The ToF data were acquired in two modes – one with the CFD in place followed

by HPTDC and RCE as is planned for the final detector (focus on the timing analysis) and one without the CFD, instead with an oscilloscope connected to the PAb output (raw data, focus on signal amplitude and correlation analysis). The analysis of the data from the measurements with the oscilloscope is the main focus of this thesis. A block scheme of the oscilloscope measurements is shown in Figure 2.7. The oscilloscope used was a LeCroy SDA760Zi.

The beam parameters

The Test Beam measurements took place at the H6 beamline in the SPS North Area (located within the CERN Prévessin site). Protons accelerated by the SPS accelerator were dumped to a target and a pion beam was then filtered from the products.

The beam was delivered in the form of periodic spills[1], each lasting for about 5 s. An example of the SPS supercycle profile is shown in Figure 2.8. The beam in the H6 beamline consists of pions (π^-) with the energy of about 120 GeV. Slight variations of the energy should not impact the measurements taken. The beam is debunched, producing a steady stream of particles instead of the usual bunch structure. The beam intensity is low, ensuring almost no pileup. The beam transverse dimension can somewhat change over time, but is usually many cm across, covering all the LQBars at once.

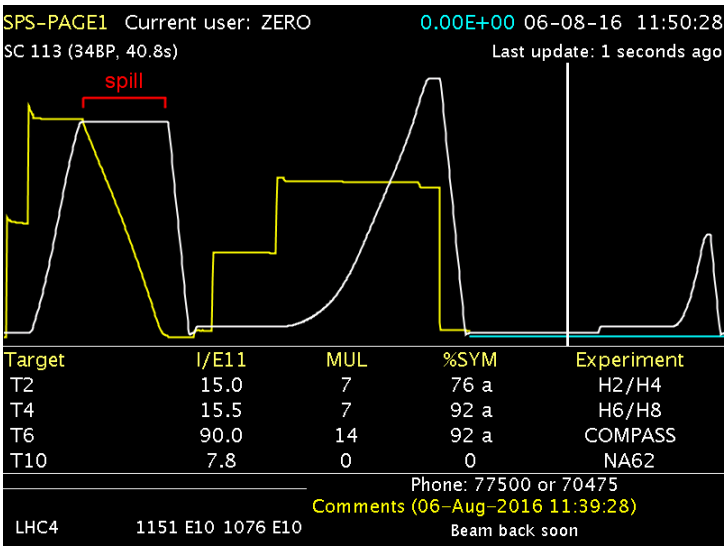

Figure 2.8: Example of the the SPS supercycle monitor. The white line represents the current through the SPS magnets (proportional to beam energy), the coloured line represents the beam intensity. The spill duration is marked in red, lasting about 5 s.

The SPS supercycle accommodates also some other users than the test area, for example the LHC filling (in the middle of the supercycle in Figure 2.8) and the machine development. This means a spill was mostly available once per supercycle, depending on its current length (usually $35 - 40$ s). The time devoted to preparing and spilling the beam for the test area is roughly the first quarter of the supercycle as seen in Figure 2.8.

[1] A spill is the time period, during which the beam is being gradually dumped from the SPS to the target, producing the pion beam entering the test area.

Chapter 3

Data processing and comparison with simulation

Only the raw data containing the PMT response waveforms gathered by the oscilloscope are the subject of the analysis in this thesis.

3.1 Data preprocessing

The raw unprocessed data contain the PMT responses for all events. An example can be seen in Figure 3.1.

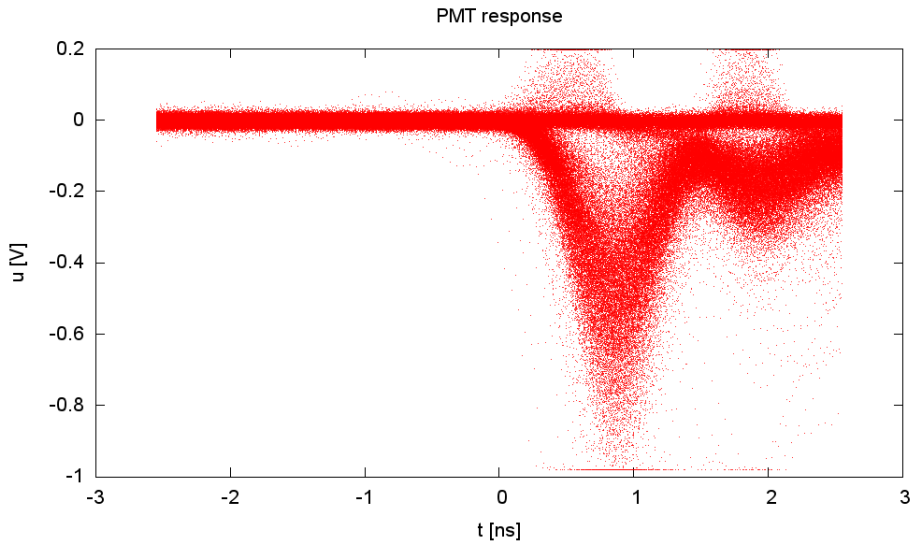

Figure 3.1: PMT responses from 400000 events laid over. A typical response peak shape with an afterpulse is clearly visible.

The raw data first got preprocessed. The amplitude of the signal, peak and edge time, edge slope and signal integral were determined, while filtering only those with a signal present at all ($u_{\min} < -50\,\mathrm{mV}$) by setting a validity flag. This information was stored in the form of a root file containing the data in the form of an n-tuple structure. The analysis was carried out almost exclusively on this preprocessed data, using the ROOT framework.

3.2 Description of the measurement scenarios

The measurements evaluated include a few different scenarios. Those scenarios will be referred to by their numbers within the ELOG system that was used for logging details about the individual measurements. There are also two different physical configurations, with the LQBars installed on different PMT channels.

There were many more measurements taken than those evaluated in this thesis, some of a technical nature (like beam alignment or tuning of the CFD threshold), some other for testing different bar designs that were rejected and many measurements with CFD, not the oscilloscope directly connected to the second pre-amplifier PAb. Those other measurements are not the subject of the analysis here.

LQBar naming convention

The individual trains are labelled by numbers 1-4. The bars constituting a train are labelled by letters A and B, where A is the bar that gets hit by a particle first. Therefore by combining these two, each bar can be assigned a name, eg. the first train consists of bars "1A" and "1B".

Oscilloscope channel mapping notation

Due to the limitation of the maximum number of active channels to four, not all bars could be measured at once. However, the oscilloscope offered an "upper" and "lower" input for each channel, allowing switching between them. The measurements on the enclosed CD are labelled "uuuu" and "llll" when all the upper or lower channels were used, or "AAAA" and "BBBB" when all the channels mapped to the first (A) or the second (B) bars were used. The train number refers to the train, which was being targeted by the triggering SiPM. The channel mapping is in Table 3.1.

Channel	Ch 1	Ch 2	Ch 3	Ch 4
u	1A	1B	2A	2B
l	3B	3A	4B	4A

Table 3.1: Channel mapping for the oscilloscope upper and lower channels.

Configuration 1

The configuration 1 (CFG1) is the measurement scenario, where the bar placement on the PMT channels is according to Figure 3.2. Each bar is placed on the channel for which it was designed, occupying the two middle columns of channels on the MCP-PMT. The top view is in Figure 3.3.

empty	1A	1B	empty
empty	2A	2B	empty
empty	3A	3B	empty
empty	4A	4B	empty

Figure 3.2: The LQBar mapping on the PMT channels with configuration 1, as seen from the back of the MCP-PMT.

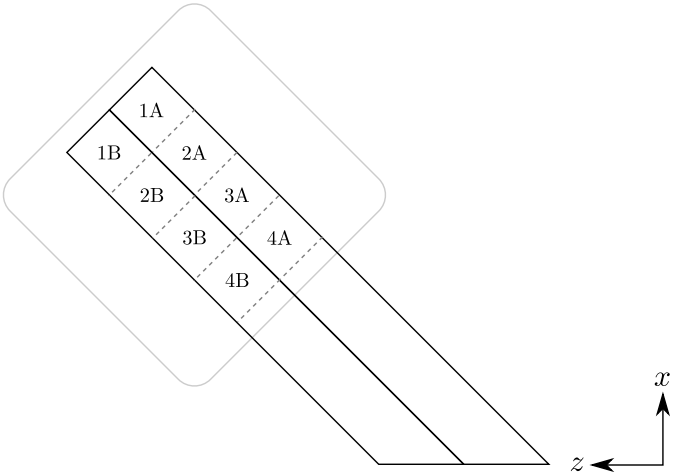

Figure 3.3: A top view of the LQBars in the configuration 1 with the PMT in the background. The beam is coming from the right in the direction of the z axis.

The configuration 1 will be used for the evaluation of the crosstalk between the neighbouring bars and their correlation, as it is a subset of the detector design.

LOG16

LOG16 measurements were focused on evaluating all the bars with many different combinations being acquired, resulting in one or two channels with an actual signal. More than two channels with a signal cannot be obtained, because there are only two bars per train. These measurements will be useful for evaluating possible crosstalk between the bars in a train as well as between the neighbouring trains.

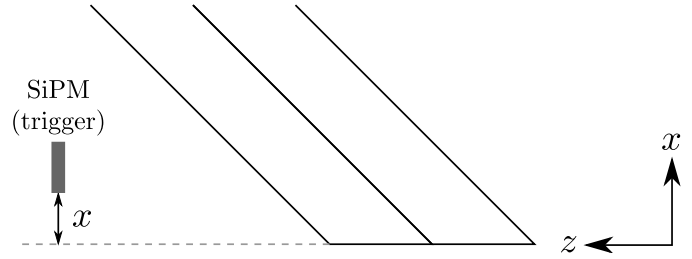

Figure 3.4: A top view of the LQBars in the configuration 1 with the SiPM x position explained.

LOG17

LOG17 measurements were the x-scan measurements, meaning that multiple different positions along the LQBar radiator were targeted by the trigger position. This allows for the evaluation of the influence the hit position has on the signal strength and optical crosstalk. The x-scan was performed by moving the triggering SiPM, as described in Figure 3.4. A position described as the "edge" position refers to the edge of the SiPM aligned with the edge of the LQbars, or $x = 0\,\text{mm}$.

The overall setup was the same as in case of LOG16, allowing for the edge and 5 mm positions to be omitted in the scan. When evaluating the LOG17 data, these measurements will be filled in from the LOG16 data.

Configuration 2

The configuration 2 (CFG2) is the measurement scenario, where the bar layout on the PMT channels is according to Figure 3.5. The "A" bars are in their corresponding channels, while the "B" bars are moved one channel further, creating a gap. Because these bars were not designed for this position, their edge is overlapping, as can be seen in Figure 3.6. In the configuration 2, the "edge" position refers to the SiPM edge aligned with the edge of the first bar, while "edge1" means the SiPM is aligned with the edge of the overlapping second bar, resulting in no signal in the first bar.

empty	1A	empty	1B
empty	2A	empty	2B
empty	3A	empty	3B
empty	4A	empty	4B

Figure 3.5: The LQBar mapping on the PMT channels with configuration 2, as seen from the back of the MCP-PMT.

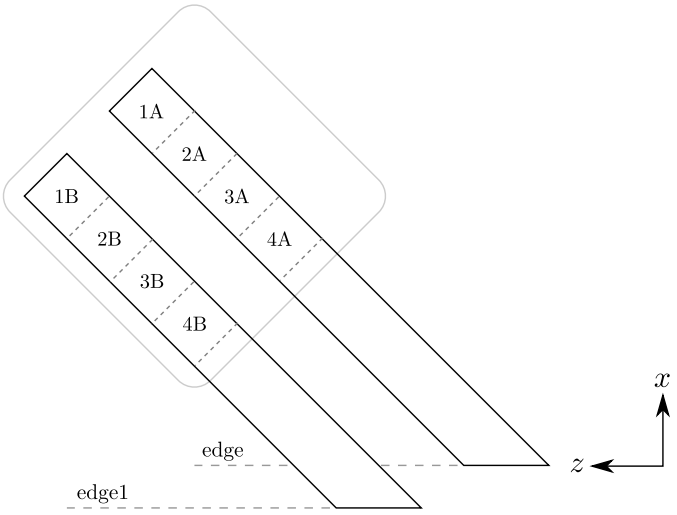

Figure 3.6: A top view of the LQBars in the configuration 2 with the PMT in the background. The beam is coming from the right in the direction of the z axis.

LOG24

The LOG24 measurements were performed in the configuration 2, but otherwise are the same as the LOG16 measurements, allowing a direct comparison. However, only the "uuuu" and "llll" combinations were measured.

LOG25

LOG25 is a PMT high voltage scan performed on the train 2. Only the train 2 on the edge position was measured.

LOG57

For the LOG57 measurements, an optical grease was applied between the LQBar end and the MCP-PMT. It allows for an evaluation of the effect the grease might have on the detector performance. All trains were measured with the SiPM on the edge and in the 5 mm position.

3.3 Simulation of the ToF bars in Geant4

The Geant4 framework is a toolkit for creating simulations of particles passing through a matter and their interactions. It operates by tracking the individual particles through the defined volumes of matter, in this case the LQBars. It is used here to perform Monte Carlo (MC) studies with high statistics or to inspect individual events.

A contribution to the development of the ToF optical part simulation was made, especially regarding output of data that proved to be necessary when analysing the results, and also minor bugfixing. However, most of the work with the simulation is simply running it with various configurations and working on the analysis of the results, not the development of the Geant4-based simulation itself. The focus is mostly on the simulation of the configurations used on the Test Beam. This means only 2 bars per train were present in the simulation.

The simulation used [11] is incapable of simulating the configuration 2 fully (the edge of the B bars would be cut to be aligned with the A bar), therefore only configuration 1 will be studied. All simulations except the x-scan were done with $x = 5$mm.

3.3.1 Visualization of Cherenkov photon tracks

Some conclusions can be made by simply observing the visualization of the simulation output. An example of such visualization is in Figure 3.7.

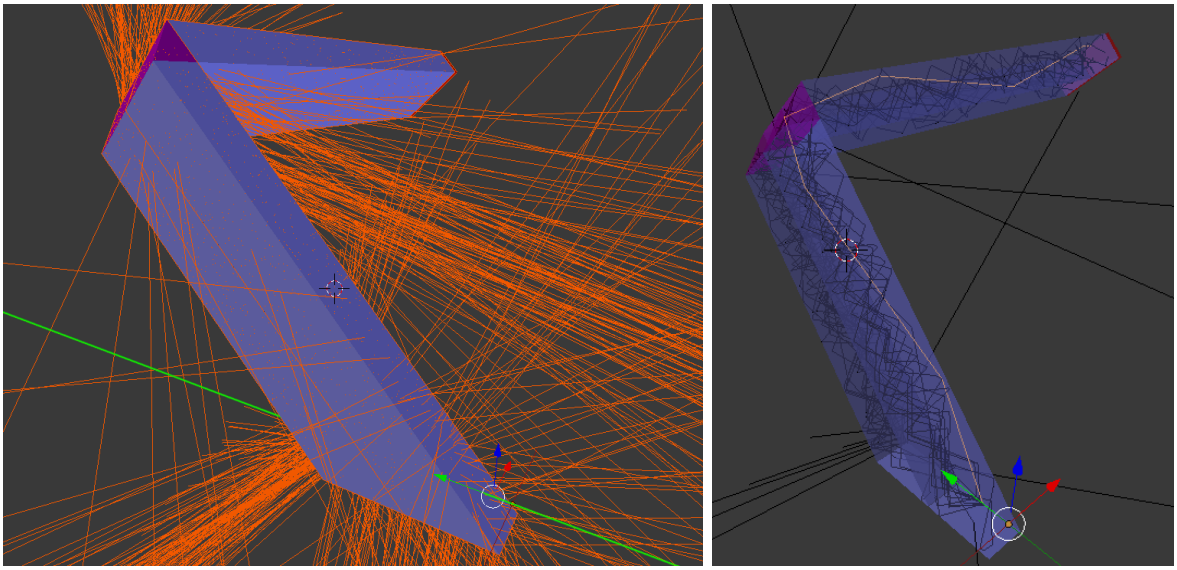

Figure 3.7: A visualization of a single particle (green) passing through two LQBars in a single train (blue). On the left, the Cherenkov photons are shown as orange lines. On the right, a subset of Cherenkov photons is shown (black) with a single photon track highlighted. The visual representation was created using the software "Blender".

On the left part of Figure 3.7, areas where a lot of Cherenkov radiation is escaping are clearly visible. It is important to note that no photons are escaping from the sides of the radiator (except for a few reflected near the ankle), as all of them fulfil the total reflection criteria on these surfaces. However, a lot of radiation is escaping near the point where the particle is leaving the last bar and many more near the ankle. Here it is important to realize that there are thee scenarios any photon can follow when reaching

the ankle, as is shown in Figure 3.8. The red path is a standard photon reflecting from the mirror, most photons ($\sim 60\,\%$) follow this scenario.

The green path is a photon that passes through the ankle without being reflected by the mirror, which usually means a low angle of incidence on the next reflection, with the total reflection criteria not fulfilled – these are the photons escaping just after the mirror. In case of a bar with a taper, many of these are gathered by reflection from the angled taper surface.

The blue path is a photon, which is reflected back to the radiator, also quite often leaving the bar. In case it stays within the bar, it will not influence the time measurement, as it cannot reach the PMT soon enough to have any effect. If it leaves the bar, it could enter the bar of the next train causing unwanted crosstalk, but the aluminium mirror on the neighbouring bar prevents that.

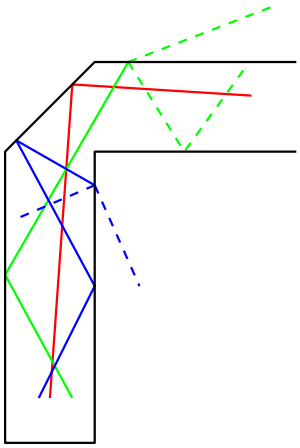

Figure 3.8: Three possible photon path scenarios near the LQBar ankle.

The photons leaving the bar near the back end of the radiator can be explained by Figure 3.9. This is the part of the Cherenkov cone which impacts the bar surface almost perpendicularly, leaving the bar. However, if another bar is present in the train, it can gather some of these photons by reflecting them from the edge. This optical crosstalk enhances the signal in the second bar, but we argue that it does not cause any correlation between the bars, the reason being each Cherenkov photon generation is an independent random event, so it is not important in which bar it is generated.

Figure 3.9 also suggests that if the particle is passing very close to the edge, the photons that would otherwise leave the bar get reflected and enhance the signal in this bar. As the passing particle gets further along x, this advantage is translated to the next bar or lost altogether. Therefore we predict a significant raw signal amplitude dependence on the x position of the particle. This is tested by analysing the simulation results as well as the measured data analysis.

Another expected effect is the influence of the x position on the time measurement. One reason is that for a higher x the photons need to travel a shorter distance, which is only partially compensated by the particle reaching the bar later. Another reason is the aforementioned reflection and gathering of photons that would otherwise leave the bar, as they reach the PMT later. In the AFP detector, these two effects will have to be countered by finding a corresponding track in the tracker and correcting for the position accordingly. In the Test Beam measurements, this is unnecessary, as the triggering area is small enough and constraints the x particle position into a 3 mm range.

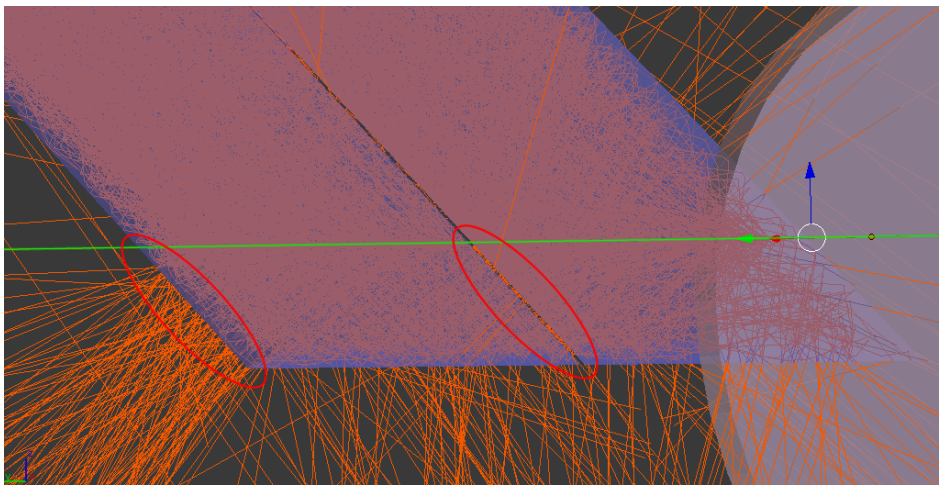

Figure 3.9: A visualization of a single particle (green) passing through two LQBars (with transparency) in a single train. The red ellipses mark the area where a lot of Cherenkov radiation is escaping the bar.

3.3.2 Dependence of timing on the x position

The dependence of timing on the x position of the particle passing through the detector can be easily shown by accumulating a histogram of the times, when the very first photon impacts the PMT. As Figure 3.10 shows, for particles further from the LQBar edge (larger x) the signal reaches the PMT sooner, as expected. The dependence is linear with roughly 4 ps/mm. The x positions used are the same as those available in the x-scan Test Beam measurements.

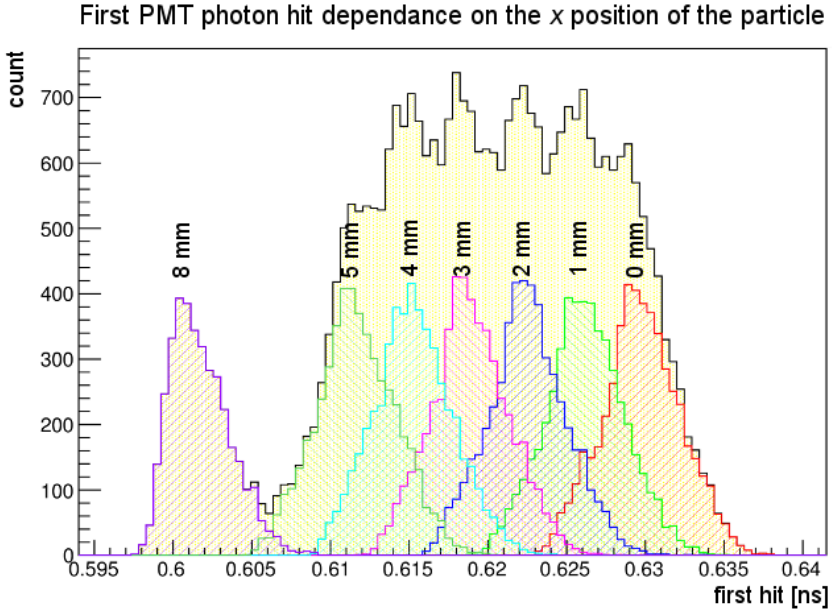

Figure 3.10: Dependence of the time the first photon reaches the PMT on the x position of the particle. Times are relative to the trigger in the simulation, placed in front of the bars. The yellow filled histogram is the sum. MC simulation.

3.3.3 Dependence of the amplitude on the x position

The amplitude of the signal is expected to be proportional to the number of photoelectrons N_{pe} created by the PMT photocathode. The simulation implements the PMT collective efficiency, enabling the number of photoelectrons to be determined.

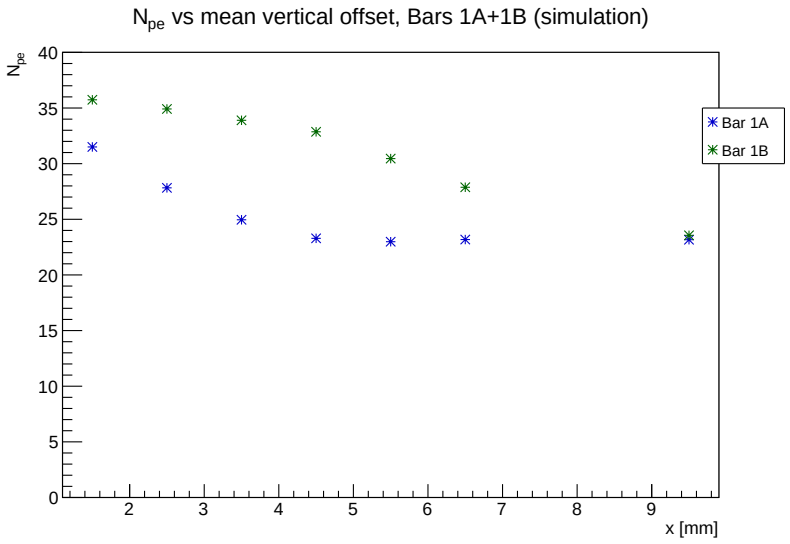

Figure 3.11: Dependence of N_{pe} on the x position. For each x position, the N_{pe} is averaged over 5000 events. The x positions are of the center of the SiPM triggering area (edge position +1.5 mm). MC simulation.

Figure 3.11 shows the dependence of the mean number of photoelectrons N_{pe} on the x position of the center of the triggering area. For the first bar, N_{pe} quickly drops with increasing x to a lower level, where it stays from about $x = 5\,\text{mm}$. This is the position, where no more photons are reflected from the edge. On the other hand, the N_{pe} decay for the second bar is much slower, as it is partially compensated by the photons from the first bar. At 8 mm (or 9.5 mm for the center), the PMT produces almost the same number of photoelectrons for both bars, while the first bar remains very slightly lower due to the longer path the photons have to travel, hence more absorption can take place.

3.3.4 Dependence of the optical crosstalk on the x position

As already discussed, the magnitude of the optical crosstalk between the bars heavily depends on the distance of the particle from the bar edge. Figure 3.12 shows the percentage of photons originating from the first bar that produced a signal in the second bar's PMT channel.

The fit in Figure 3.12 shows that the maximum volume of optical crosstalk occurs for particles passing 4.3 mm from the bar edge, peaking at 28 %. At 9.5 mm, no more photons from the first bar get captured by the second one. However, if a third bar was present, the crosstalk percentage would be close to the peak for it here.

The optical crosstalk is explained by the mechanism described by Figure 3.9 on page 27. In the opposite direction (from bar B to bar A), the optical crosstalk is almost none ($< 0.1\,\%$, meaning much less than one photon per event). The optical

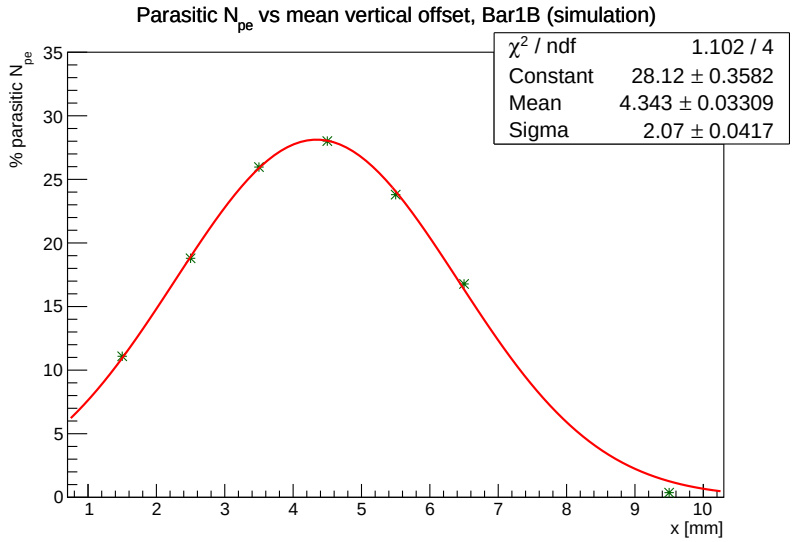

Figure 3.12: Dependence of the optical crosstalk on the x position. The x positions are of the center of the SiPM triggering area (edge position +1.5 mm). MC simulation.

crosstalk between neighbouring trains is virtually zero due to all photons fulfilling the total reflection criteria on the sides of the radiator.

3.3.5 Time distribution of photons hitting the PMT

The distribution of photon hits in time is an important property of the ToF detector optical part. In the ideal case, all photons would reach the PMT simultaneously. In the reality however, they are spread due to various directions along the Cherenkov cone and due to variability of wavelengths and corresponding indexes of refraction affecting their speed (dispersion). The PMT response is greatly influenced by this distribution, this in turn affects the timing resolution.

There are some important differences between the bars with a taper (the first train) and those without it. The taper captures some photons that would otherwise escape the bar, while also "speeding them up" by making their trajectory more direct. This results in a slightly better timing resolution of the tapered train.

The time distribution of photon hits for the first train (with taper) is in Figure 3.13. We can see that the crosstalk influence in the bar B comes into effect slightly later, which is the same also for the second train in Figure 3.14. Compared to each other however, the tapered train produces a smoother distribution.

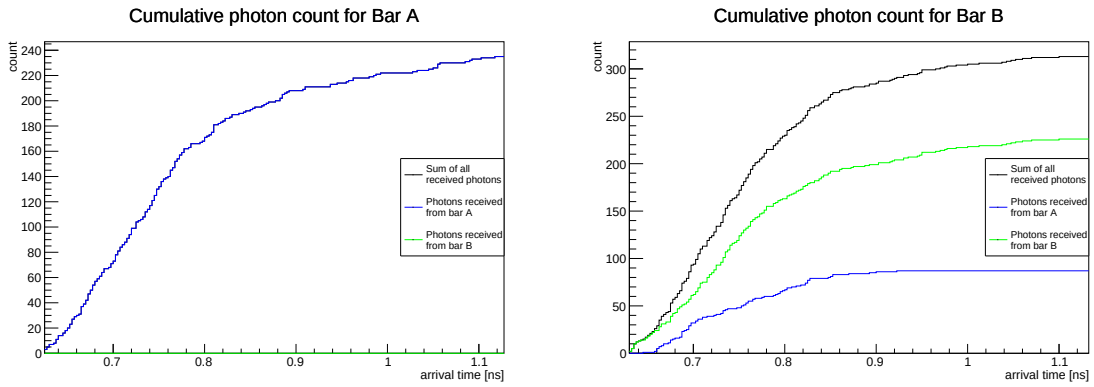

Figure 3.13: A single event cumulative photon count for the bars in the first train.

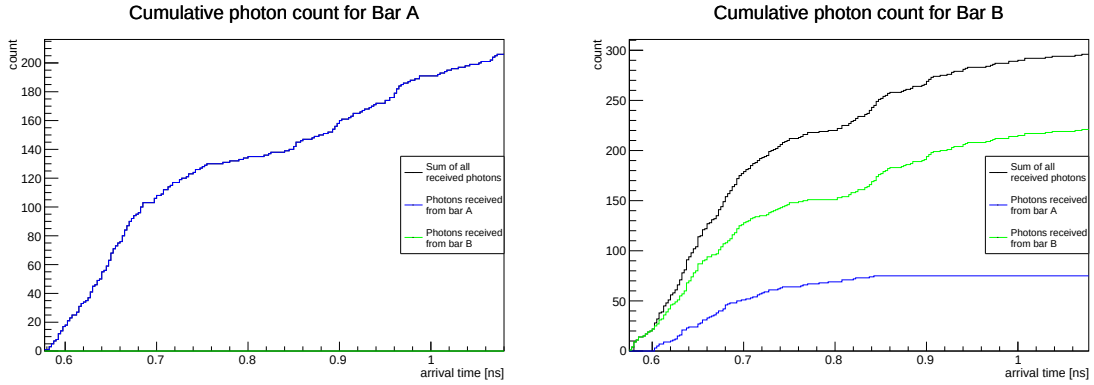

Figure 3.14: A single event cumulative photon count for the bars in the second train.

The apparent gap in the untapered train is caused by the missing photons that the taper gathers. The overall photon count is not too dramatically changed, but since the fastest photons have the most influence on the timing resolution, the effect of the taper is noticeable in the overall timing resolution. The taper forces the bar to be thinner, therefore we cannot use it on all trains, otherwise the ToF detector would not cover the whole tracker acceptance.

3.4 Analysis of the Test Beam data

The data used for the analysis are the preprocessed raw data as discussed in section 3.1. The raw PMT response can be seen in Figure 3.1 on page 21, it is a negative voltage response.

Because the peak is negative, the strongest response of the PMT (the highest amplitude) is the lowest drop in voltage into the negative values, therefore the minimum. The preprocessed data in the root file format contain for each event:

- validity flag `idv` (signal is valid, amplitude $u_{\min} < -50\,\mathrm{mV}$),
- edge time `tp` (the time, when the leading edge of the negative peak falls),
- edge slope `esl` (slope of the leading edge),
- signal amplitude `pl` (the signal peak voltage),
- peak time `pt` (time when peak occurred),
- signal integral `a` (area under the curve).

From these values, the amplitude is of the most concern, reflecting the optical signal strength. This can be used to evaluate the signal strength dependence on the x position or to compare the measurements with or without a grease applied. The correlation of amplitudes of the bars in a train can be also used to determine whether a crosstalk affecting the measurements is present. Peak or edge time could in principle be used to evaluate the timing resolution, but it suffers from poor precision. The measurements with CFD provide much better data for this purpose.

3.4.1 Cuts

There are multiple cuts that were used to clean up the data. The first obvious cut is the `idv` validity flag, which gets rid of most of the empty triggers. After using only this cut, the signal amplitude histograms were evaluated, an example is in Figure 3.15.

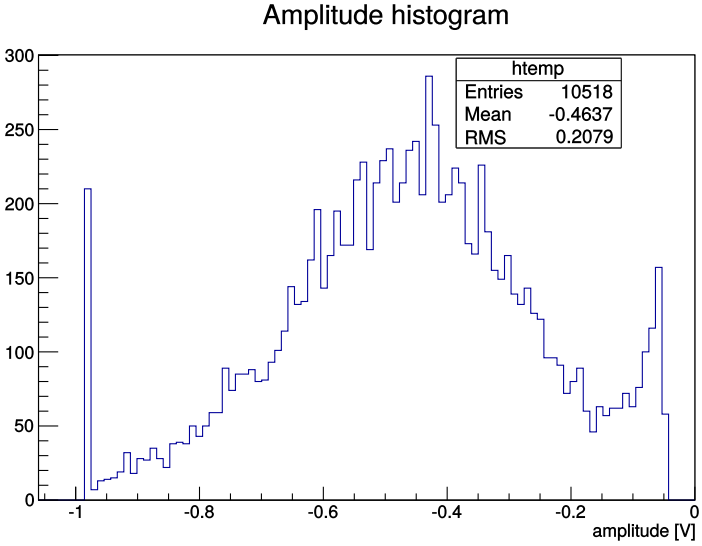

Figure 3.15: A typical signal amplitude histogram. The tall peak on the left is the underflow bin.

Amplitude cuts

It is necessary to do two cuts on the amplitude: remove the first non-empty bin (the underflow bin) and also cut off the pedestal on the right near zero. The pedestal is the background noise. It's position somewhat varies for different measurements, also sometimes it is more pronounced than in some other measurements. Therefore a reliable method for pedestal position detection had to be devised. It works by first fitting a Gaussian through the roughly estimated signal part and then adding a quadratic pedestal fit. The resulting function shape is in Figure 3.16. The minimum between the signal shape and the pedestal then serves as the basis for a cut, which is applied at 5/6 of the distance between the fitted peak of the useful signal and the minimum. Another useful information from this fit is the range, which will be used for a subsequent histogram fit. A missing signal detection is also done to prevent working with noise only. The relevant code performing this fit is on the enclosed CD in the file `TB_data/analysisCode/amplitudecutoff.cxx`.

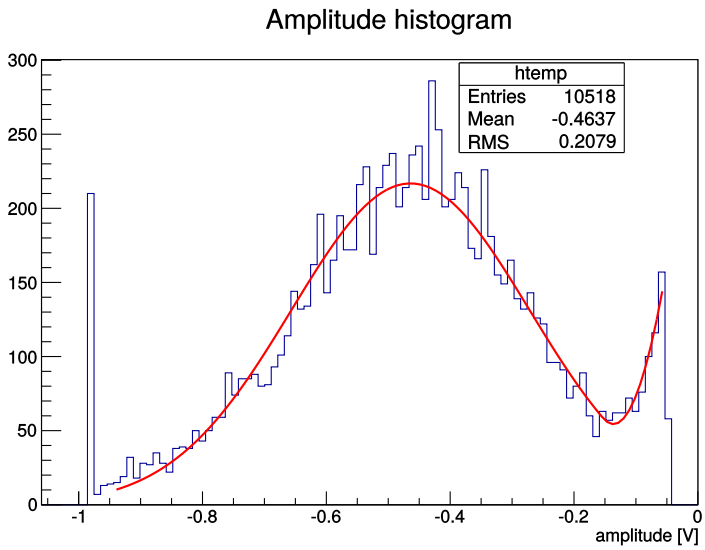

Figure 3.16: An example of an amplitude signal and the pedestal fit used to determine the cut position.

Peak time cut

The peak time cut is necessary due to a second small peak in the peak time distribution. This second peak as seen in Figure 3.17 is caused by the afterpulse visible in Figure 3.1 on page 21. Occasionally, this afterpulse can overshoot the primary pulse and be evaluated by the preprocessing code instead of the primary pulse. The amplitude cut already removed a significant portion of these events, as they are more likely to occur when the amplitude is low.

These are obviously undesired events. The cut is based on the main peak fit and applied at 4σ. After applying this cut, the amplitude histogram was affected slightly at lower amplitudes, further confirming that the afterpulse overshoot is much more likely at small amplitudes.

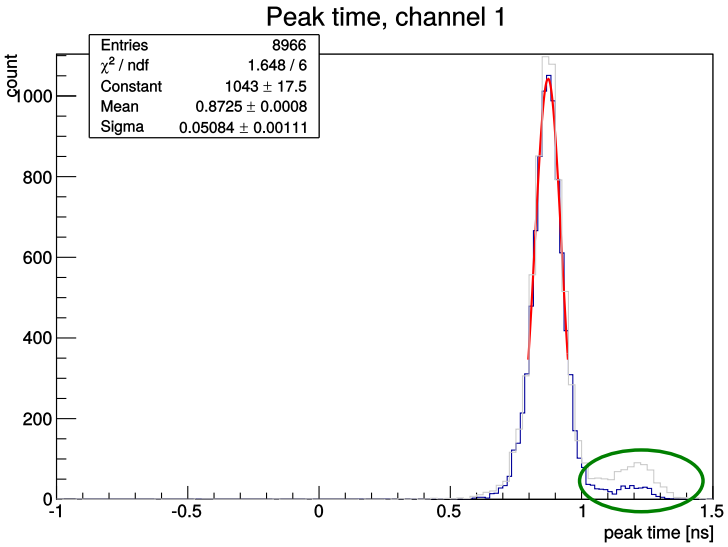

Figure 3.17: Explanation of the peak time cut. The green ellipse marks the small peak caused by the afterpulses. The gray histogram is before the amplitude cut.

Edge time cut

After these cuts, some noise still remains in the edge time histogram. This could influence the correlation plots, so a cut is applied with the same logic as the peak time cut – at 4σ based on the main peak fit.

Amplitude histogram after the cuts

The amplitude histogram typical appearance after these cuts were applied can be seen in Figure 3.18. The original uncut histogram is shown in gray (it had to be rescaled due to a finer binning, so it is only for reference). The cut pedestal and omitted underflow bin are clearly visible, as well as the chosen fit range.

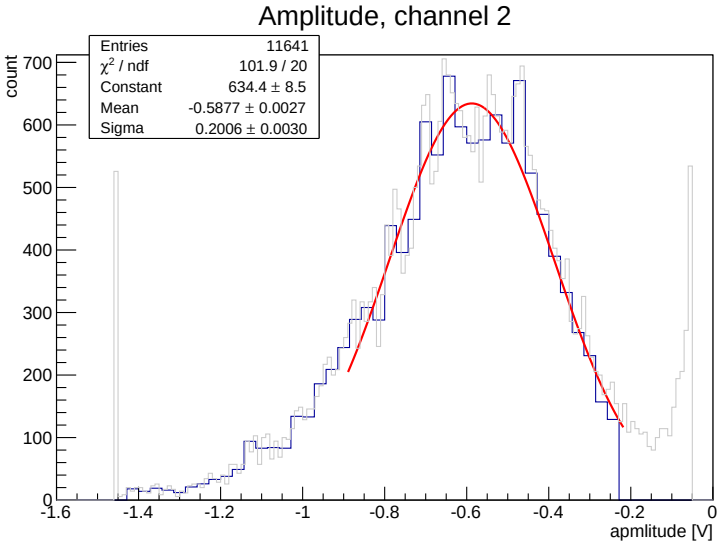

Figure 3.18: A typical amplitude histogram after the cuts were applied. The gray histogram is the original without cuts.

Pedestal

A typical pedestal shape is shown in Figure 3.19. The pedestal counts quickly drop for higher PMT responses (lower voltages), with almost no events below $-0.2\,\mathrm{V}$. Therefore the influence on the amplitude histogram fit should be minimal.

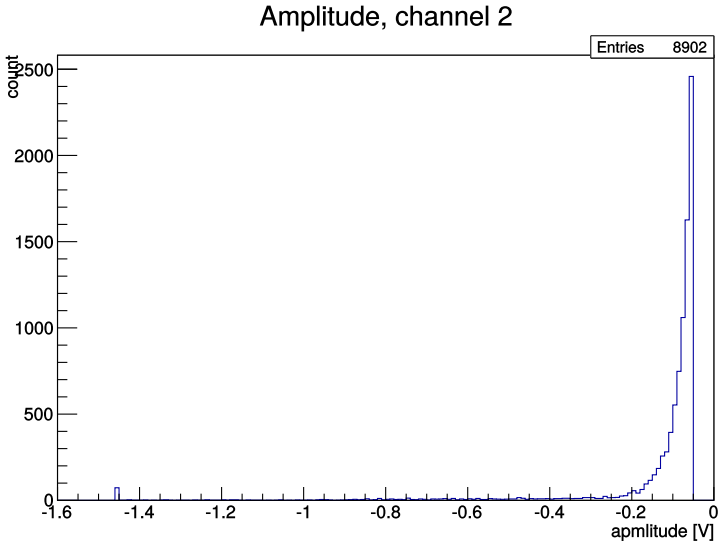

Figure 3.19: A typical amplitude pedestal measured by a channel, for which there was no trigger. The triggering area was aligned with a different train during this measurement.

In theory the pedestal could be subtracted, but such approach would introduce errors due to it's variability. A static cut would affect some cases, where the amplitudes are low and very close to the pedestal. This is the reason why the above described approach for the amplitude cut position search was developed.

Amplitude correlation plot cut

The amplitude correlation plots were suffering from isolated events far from the core, which could influence the overall correlation by having a long lever arm. A cut was devised, killing all bins with less than 10 % of the maximum bin content. This way only the core with many events is evaluated (Figure 3.20).

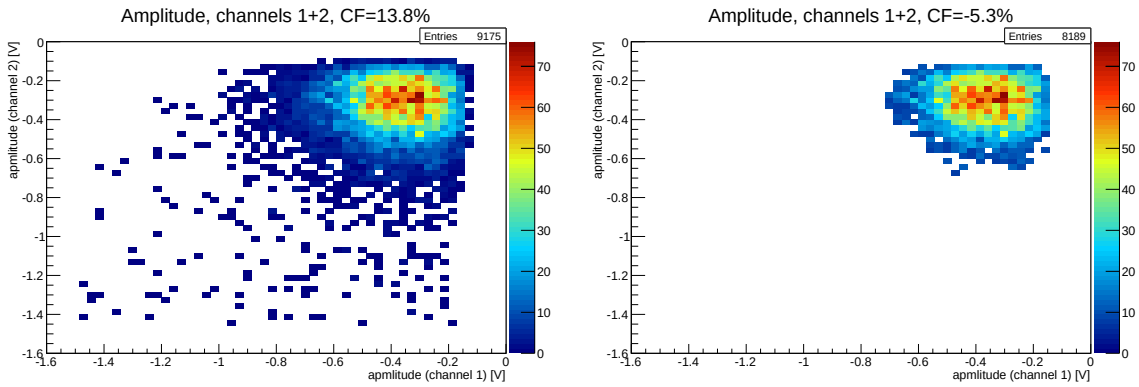

Figure 3.20: Comparison of amplitude correlation plots before and after the cut.

3.4.2 Analysis code

The analysis code performing the above mentioned cuts and producing histograms and correlation plots is placed in the folder `TB_data/analysisCode` on the enclosed CD. It is accompanied by a `Makefile` producing an executable `rawAnalysisTB` and bash scripts for easy execution of the analysis on the whole dataset.

The output of this analysis code is a PDF file with the histograms for all the available data and correlation plots if at least two channels contain a valid data (not only pedestal). It also creates a text file `amplitude.dat` with the amplitudes determined by fitting the amplitude histograms, thus giving the modus of each amplitude distribution.

3.4.3 Analysis of the LOG16 data

The complete analysis output of all LOG16 measurements can be found on the enclosed CD in the folder `TB_data/LOG16`, the text file `TB_data/Amplitudes_LOG16.txt` contains the accumulated amplitude data for all LOG16 measurements.

measurement	1A	1B	2A	2B	3A	3B	4A	4B
edge u,l	-0.4673	-0.6388	-0.2971	-0.4454	-0.3724	-0.5578	-0.3907	-0.6503
edge A,B	-0.5200	-0.7156	-0.3331	-0.5097	-0.4218	-0.6259	-0.3747	-0.6255
5mm u,l	-0.3500	-0.5869	-0.2070	-0.4364	-0.2773	-0.5315	-0.2426	-0.5342
5mm A,B	-0.3480	-0.5836	-0.2024	-0.4325	-0.2777	-0.5253	-0.2462	-0.5382

Table 3.2: Amplitudes in all bars for the LOG16 measurements. The color intensity is proportional to the amplitude value. All values are in [V].

All the LOG16 measurement results in Table 3.2 show that the second bar in a train always receives significantly more optical signal, resulting in a stronger PMT response. The increase as a percentage of the first bar's amplitude is in Table 3.3.

measurements	Train 1	Train 2	Train 3	Train 4
edge u,l	27 %	33 %	33 %	40 %
edge A,B	27 %	35 %	33 %	40 %
5mm u,l	40 %	53 %	48 %	55 %
5mm A,B	40 %	53 %	47 %	54 %

Table 3.3: Increase in amplitude of B bars compared to A bars

It is easy to notice certain discrepancies in Table 3.2. All edge measurements except for train 4 exhibit significantly larger amplitudes during the A,B measurements than during the u,l measurements. The measurements were done in this order:

1. edge, train1 → train4, uuuu/llll,
2. 5 mm, train1 → train4, uuuu/llll,
3. edge, train1 → train4, AAAA,
4. 5 mm, train1 → train4, AAAA,
5. edge, train1 → train4, BBBB,
6. 5 mm, train1 → train4, BBBB.

Therefore we cannot explain this difference by any shift in time.

The measurement setup was exactly the same, except for one thing – the oscilloscope voltage scale. The used voltage scales during LOG16 measurements are in Table 3.4. Those equivalent measurements, where the voltage scale was unchanged, do not exhibit any change in measured amplitudes in Table 3.2.

Edge								
mV/div	1A	1B	2A	2B	3A	3B	4A	4B
UUUU/LLLL	130	130	130	130	150	150	300	300
AAAA/BBBB	200	200	200	200	300	300	300	300
5 mm								
mV/div	1A	1B	2A	2B	3A	3B	4A	4B
UUUU/LLLL	200	200	200	200	300	300	300	300
AAAA/BBBB	200	200	200	200	300	300	300	300

Table 3.4: Voltage scales used on the oscilloscope during the LOG16 measurements. The green background marks those equivalent pairs of measurements, where the scale was unchanged.

A direct comparison of the equivalent measurements is in Table 3.5. The difference and the ratio are shown with the background color denoting the magnitude of the discrepancies.

LOG16 difference

x	combination	1A	1B	2A	2B	3A	3B	4A	4B
edge	(u,l) – (A,B)	0.0527	0.0768	0.0360	0.0643	0.0494	0.0680	-0.0160	-0.0248
5mm	(u,l) – (A,B)	-0.0020	-0.0033	-0.0045	-0.0039	0.0004	-0.0062	0.0036	0.0040

LOG16ratio

x	combination	1A	1B	2A	2B	3A	3B	4A	4B
edge	(A,B) / (u,l)	1.113	1.120	1.121	1.144	1.133	1.122	0.959	0.962
5mm	(A,B) / (u,l)	0.994	0.994	0.978	0.991	1.001	0.988	1.015	1.008

Table 3.5: Amplitude difference and ratios for equivalent measurements.

By comparing the two amplitude histograms from the equivalent measurements, Figure 3.21 is obtained. One of the histograms (blue) is from the 130 mV/div measurement, the other (red) from the 200 mV/div measurement. The differences are obvious.

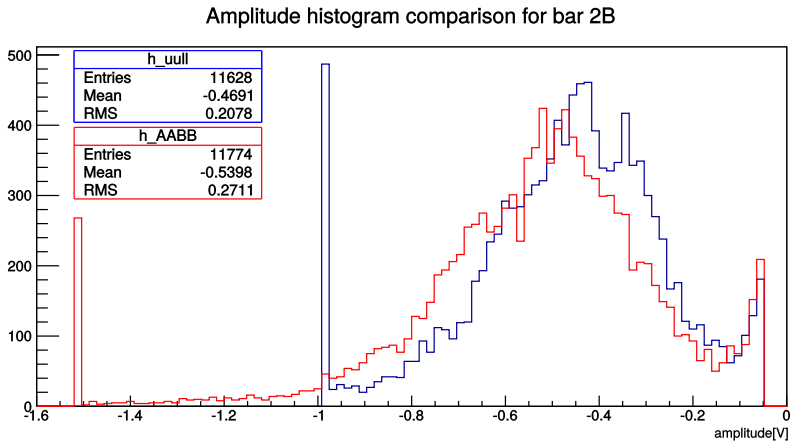

Figure 3.21: Comparison of equivalent measurements for bar 2B on the edge.

By rescaling the values filled into one of the histograms by the ratio of the amplitudes determined from fit, it is possible to check whether the problem might be with incorrect fitting. The resulting comparison is in Figure 3.22. The blue histogram on the right contains values scaled up by 1.140. By doing this, the histograms nicely overlap, proving that the discrepancy cannot originate from the amplitude histogram fit.

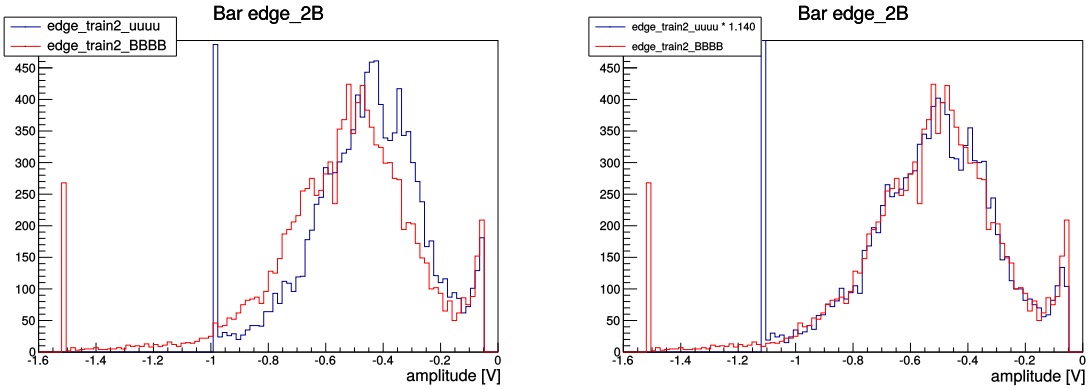

Figure 3.22: Comparison of amplitude histograms for equivalent measurements of bar 2B on edge. The filled values were rescaled on the right blue histogram.

The most likely explanation of the differences with changing oscilloscope scale is miscalibration. Care needs to be taken to compare only those measurements, where the used voltage scale of the oscilloscope remains the same, otherwise an appropriate correction factor needs to be calculated and applied.

3.4.4 Analysis of the x-scan (LOG16 + LOG17 data)

The complete analysis output of all LOG17 measurements can be found on the enclosed CD in the folder `TB_data/LOG17`, the text file `TB_data/Amplitudes_LOG17.txt` contains the accumulated amplitude data for all LOG17 measurements.

The LOG17 measurements were done only for the first two trains. By combining it with some of the LOG16 data, results for $0 - 5$ mm with 1 mm step and for 8 mm can be obtained. These results are in Table 3.6 with a corresponding graph in Figure 3.23.

x [mm]	1A [V]	1B [V]	2A [V]	2B [V]
0	−0.468	−0.640	−0.298	−0.445
1	−0.492	−0.711	−0.307	−0.489
2	−0.459	−0.676	−0.267	−0.487
3	−0.408	−0.655	−0.229	−0.470
4	−0.384	−0.620	−0.214	−0.462
5	−0.352	−0.588	−0.207	−0.437
8	−0.348	−0.469	−0.200	−0.333

Table 3.6: Amplitudes for x-scan measurements.

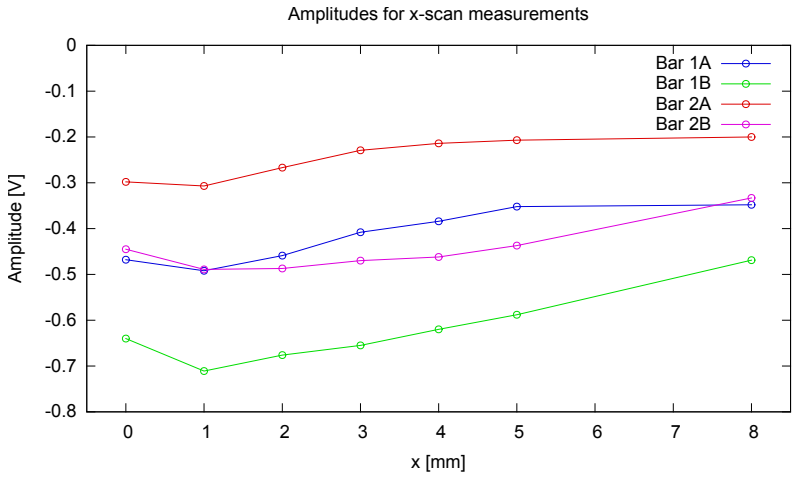

Figure 3.23: Amplitudes for various distances from the bar edge during x-scan.

The amplitudes are decreasing with increasing distance from the edge, as is expected due to reduced amount of photons being reflected from the edge. For the B bars however, the x increase induces increase in amplitude at first, because it gathers some signal escaping from the first bar. The first train produces overall stronger signal compared to the second train thanks to the taper.

Another interesting parameter to look at during the x-scan is the correlation of amplitudes between the bars in a train. An example of a correlation plot is in Figure 3.24. These correlation plots were used to calculate the correlation factors in Table 3.7 with a corresponding plot in Figure 3.25.

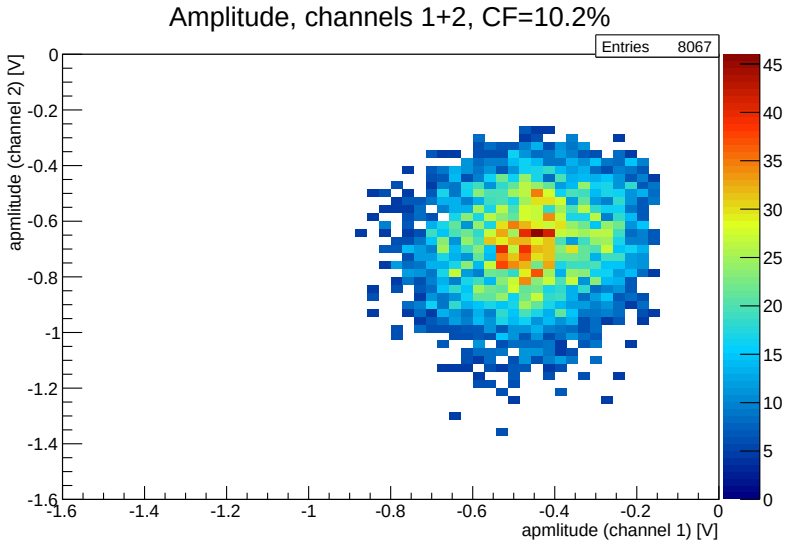

Figure 3.24: An example of a correlation plot for x-scan (train 1 at $x = 2\,\mathrm{mm}$).

x [mm]	Train 1 [%]	Train 2 [%]
0	9.8	12.1
1	12.2	12.2
2	10.2	11.0
3	10.6	10.9
4	9.1	5.7
5	7.1	6.6
8	9.3	7.3

Table 3.7: Correlations of amplitudes for the x-scan measurements.

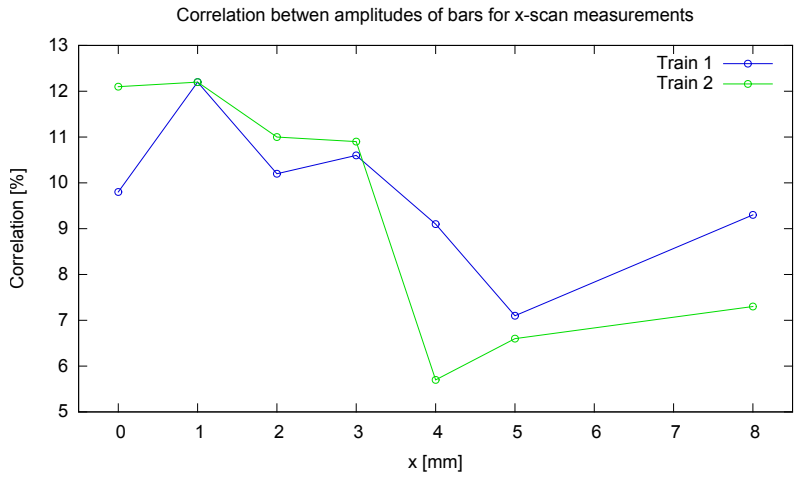

Figure 3.25: Correlations of amplitudes for the x-scan measurements.

The correlation factor dependence on the x position in Figure 3.25 is mostly decreasing with increasing distance from the bar edge. This confirms that the optical crosstalk (peaking between 4 and 5 mm) does not cause an increase of the correlation, on the contrary the more optical crosstalk, the less correlation we observe.

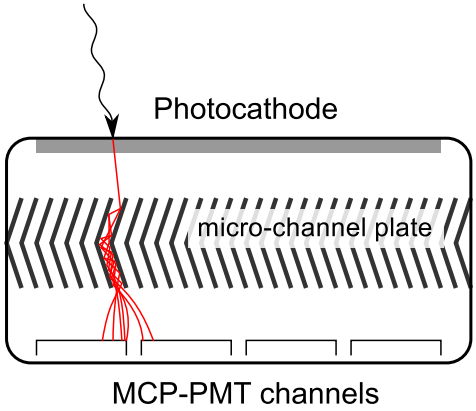

Figure 3.26: The charge sharing mechanism within the MCP-PMT.

Another source of correlation must be considered, especially within the PMT and the electronics. An important potential source of a crosstalk inducing a correlation

is the charge-sharing within the MCP-PMT. The charge sharing can occur, when the photon hits the photomultiplier near the edge of a channel, as explained in Figure 3.26. Some of the generated electrons can impact the neighbouring channel, inducing correlations. This effect can be mitigated by reducing the anode gap. The final ToF detector will be using an MCP-PMT with this modification.

The x-scan measurements are an opportunity to examine the stability of the PMT signal. A comparison between the signal amplitude and the signal area can reveal potential signal shape changes. This comparison for train 1 is in Figure 3.27. As can be seen, there is a near perfect correlation between the signal amplitude and the signal area, even when data from both bars are combined. Therefore there are no significant changes in the PMT response shape that could affect the measurements.

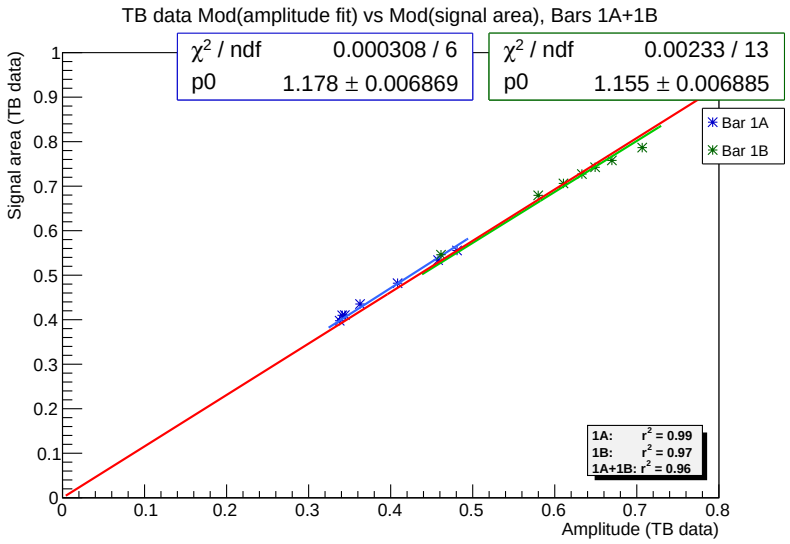

Figure 3.27: Comparison of the signal amplitude and the signal area during x-scan.

3.4.5 Analysis of the LOG24 data (CFG2)

The complete analysis output of all LOG24 measurements can be found on the enclosed CD in the folder `TB_data/LOG24`, the text file `TB_data/Amplitudes_LOG24.txt` contains the accumulated amplitude data for all LOG24 measurements.

The LOG24 measurements were acquired in the configuration 2, where the B bars were moved one channel further from the A bars, creating a gap. While they are not exactly equivalent to the final ToF bars due to the overlapping bar edge, these measurements can be used for evaluation of the correlation between the bars in a train that are not directly neighbouring and comparison with the LOG16 measurements.

The LOG24 measurements were taken with 300 mV/div scale on the oscilloscope, so only a subset of the measurements from LOG16 with the same scale setting is used for the comparison.

From the edge measurements, this is only the train 4. The amplitude comparison is in Table 3.8. Compared to the considerable increase in amplitude in the second bar in configuration 1, the amplitude in the second bar for configuration 2 is almost the same as in the first one. This is caused by the missing optical crosstalk. By comparing the correlation factors for amplitudes of the bars, in CFG1 there is a very slight correlation of 10.7 %, while in CFG2 the correlation factor is −4.0 % (anticorrelation).

configuration	4A	4B
1	-0.3911	-0.6503
2	-0.2420	-0.2757

Table 3.8: Comparison of the CFG1 and CFG2 edge measurements for train 4.

A comparison of the 5 mm measurements is possible for the trains 3 and 4. The results in Table 3.9 are very similar to the edge measurements – the second bar does not receive any additional signal due to the optical crosstalk in case of CFG2, resulting in much more similar amplitudes compared to the first bar. The correlation factors are in Table 3.10, the CFG2 has less correlation, even dropping into anticorrelation. This is due to the gap, which prevents charge sharing from producing any correlation as in case of the neighbouring channels.

configuration	3A	3B	4A	4B
1	-0.278	-0.532	-0.243	-0.534
2	-0.192	-0.230	-0.145	-0.290

Table 3.9: Comparison of the CFG1 and CFG2 5 mm measurements for trains 3 + 4.

configuration	Train 3 [%]	Train 4 [%]
1	9.8	7.7
2	-5.4	-2.9

Table 3.10: CFG1 and CFG2 amplitude correlations for trains 3 + 4.

3.4.6 Analysis of LOG25 data (high voltage scan)

The complete analysis output of all LOG25 measurements can be found on the enclosed CD in the folder `TB_data/LOG25`, the text file `TB_data/Amplitudes_LOG25.txt` contains the accumulated amplitude data for all LOG25 measurements.

The LOG25 is a PMT high voltage scan performed on the edge of the train 2. The results are in Table 3.11 with a corresponding Figure 3.28. As expected, the amplitudes are increasing for higher HV, with both bars performing very similarly due to the gap preventing optical crosstalk. HV = 1870 V was used for all the other runs as the optimal voltage level.

PMT HV [V]	2A [V]	2B [V]
1850	−0.199	−0.213
1870	−0.257	−0.271
1900	−0.408	−0.409
1930	−0.576	−0.552

Table 3.11: Amplitudes of the PMT responses during the high voltage scan.

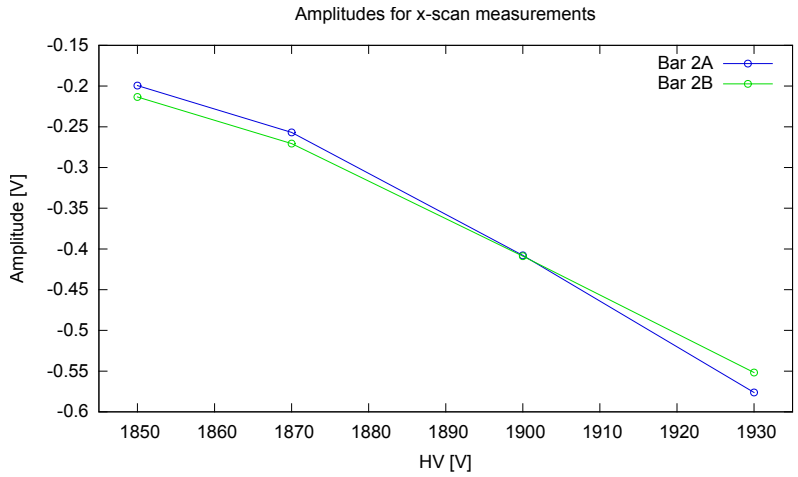

Figure 3.28: Amplitudes of the PMT responses during the high voltage scan.

3.4.7 Analysis of the grease effect (LOG57 and LOG24)

The complete analysis output of all LOG57 measurements can be found on the enclosed CD in the folder `TB_data/LOG57`, the text file `TB_data/Amplitudes_LOG57.txt` contains the accumulated amplitude data for all LOG57 measurements.

The LOG57 measurements were acquired with optical grease applied between the bar light guide end and the MCP-PMT. This ensures a better optical signal transmission (less photons reflected by the bar end). The LOG57 measurements were however acquired with 200 mV/div oscilloscope scale, while LOG24 was acquired with 300 mV/div scale. This needs to be compensated for by a factor of ~ 1.25 based on the LOG16 results, allowing direct comparison.

LOG24 300mV/div

x	1A	1B	2A	2B	3A	3B	4A	4B
edge	-0.3584	-0.3015	-0.1984	-0.2219	-0.2928	-0.1976	-0.2417	-0.2743
5mm	-0.2371	-0.3169	-0.1376	-0.2291	-0.1912	-0.2303	-0.1439	-0.2884
edge1		-0.3642		-0.2742		-0.2742		-0.3358

LOG57 compensated for 300mV/div factor 1.24874

x	1A	1B	2A	2B	3A	3B	4A	4B
edge	-0.7239	-0.6226	-0.4254	-0.6181	-0.4150	-0.6363	-0.6394	-0.4721
5mm	-0.5527	-0.6596	-0.3305	-0.6658	-0.3010	-0.6944	-0.4769	-0.5155
edge1		-0.6948		-0.6386		-0.6589		-0.4974

LOG57-LOG24 diff compensated

x	1A	1B	2A	2B	3A	3B	4A	4B
edge	-0.3656	-0.3211	-0.2270	-0.3962	-0.1223	-0.4387	-0.3978	-0.1978
5mm	-0.3156	-0.3427	-0.1929	-0.4367	-0.1097	-0.4641	-0.3330	-0.2272
edge1		-0.3306		-0.3644		-0.3847		-0.1617

LOG57/LOG24 ratio compensated

x	1A	1B	2A	2B	3A	3B	4A	4B
edge	2.0202	2.0652	2.1442	2.7859	1.4177	3.2198	2.6460	1.7209
5mm	2.3308	2.0814	2.4012	2.9062	1.5739	3.0156	3.3136	1.7877
edge1		1.9077		2.3289		2.4029		1.4815

Table 3.12: The effect of the optical grease on the signal amplitude. LOG24 was without the grease while LOG57 with the grease applied. The background colour reflects the amplitude values and the magnitude of differences between the measurements.

The effect of the optical grease is analysed in Table 3.12. The ratio of the amplitudes with and without the grease ranges from ~ 1.5 up to over 3, probably depending on the quality of the contact between the LQBar surface and the PMT with the grease between them. The effect is very significant, the guess being that the large portion of less directly travelling photons (with many internal reflections) is affected by the grease the most, as the probability they will be reflected by the light guide end is lowered. However, grease usage in the secondary vacuum inside the Roman Pot could be problematic and the influence on the timing resolution is not very high.

It is also interesting to note that the A bar amplitudes drop when moving from the edge to 5 mm, but the B bar amplitudes do not, because they extend much lower and their edge is not helping near the A bar edge position in the first place. The edge effect is noticeable on the B bars only near the edge1 (the B bar overlapping edge position). On the edge1, no signal is in the A bars, as explained by Figure 3.6 on page 24.

3.5 Comparison of measured data and simulation

3.5.1 Crosstalk between the trains

The simulation results regarding the crosstalk between trains agree with the data. No signal was detected in the trains not targeted by the trigger in any of the measurements performed. The charge sharing within the PMT is not strong enough by itself to introduce any directly measurable crosstalk signal of this kind, only pedestal was seen in the trains not currently covered by the trigger.

3.5.2 Crosstalk between bars from a single train

The optical crosstalk between bars within a train is very strong, depending on the x position along the radiator accounting for up to 55 % increase in the measured amplitude. Simulation predicts optical crosstalk up to $\sim 30\,\%$, but other effects of the measurement equipment like the charge sharing and crosstalk within the amplifiers could influence the measured difference between the bars. A physical contact between the bars can also cause the photons to reach the other bar more easily.

As predicted by the simulation (Figure 3.11 on page 28), the amplitude depending on the x position starts dropping at larger x for the second bars in a train (Figure 3.23 on page 38). This is due to a partial compensation by the optical crosstalk building up in the second bar.

3.5.3 The effect of the taper

The taper on the first train helps to gather more photons and guide them to the PMT. As predicted by the simulation, the amplitudes in the first train are always higher than for the other trains, as can be seen in Table 3.2 on page 35. The effect of the taper on the time distribution of photon hits has no counterpart for a direct comparison in the measurements, but together with the higher amplitude results in a slightly better timing resolution.

3.5.4 Signal amplitude during the x-scan compared to the number of photoelectrons from simulation

If we presume linear response of the PMT, we can compare the number of photoelectrons N_{pe} from simulation to the measured amplitudes. The x-scan measurements provide useful changing scenario to evaluate whether there is a strong correlation of the simulation and measurement.

The comparison is in Figure 3.29, where we can see the results are not very good. There is some correlation for individual bars, but the different bars exhibit a different ratio between the simulation N_{pe} and the measured amplitude.

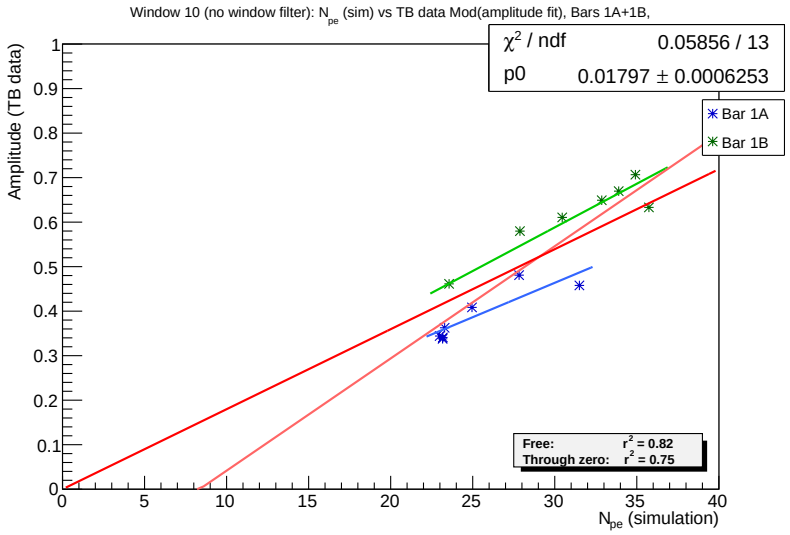

Figure 3.29: The correlation between the number of photoelectrons predicted by the simulation for the first train and the measured amplitudes during the x-scan. All photons are accounted for by the simulation.

This can be mostly corrected by introducing a time window limitation on the incoming photons in the simulation. Multiple different window durations were evaluated, see the plots in the file `TB_sim/xscan_sim/xscan_TBdata_Sim_comparison.pdf` on the enclosed CD. In Figure 3.30, only those reaching the PMT within 250 ps of the first photon hit are included in the simulation. This very roughly approximates the PMT response, where photons arriving too late no longer influence the peak. By doing this, the behaviour of the first and the second bar are much better aligned. However, the simulation still tends to underestimate the N_{pe} for the second bar, which could be explained by the bars slightly touching in reality, enabling a bit more of optical crosstalk to occur.

A realistic model of the PMT is needed for a better simulation of the measurement, while the 250 ps window offers decent results for the moment.

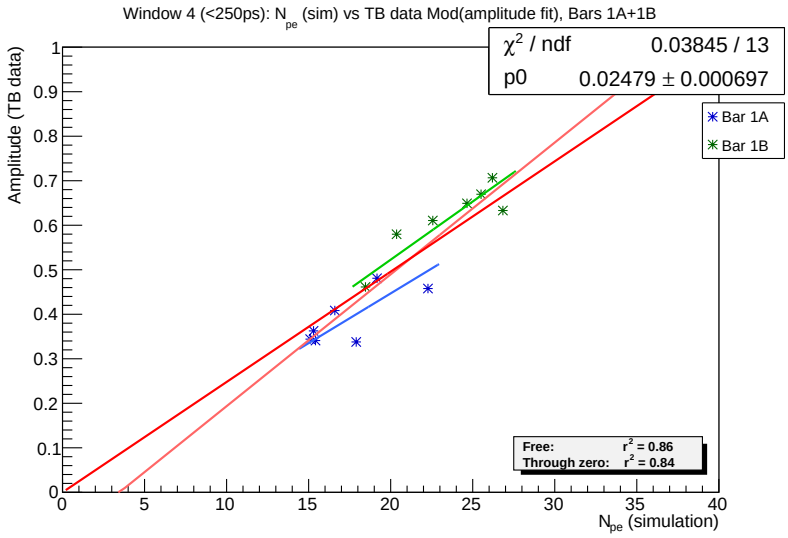

Figure 3.30: The correlation between the number of photoelectrons predicted by the simulation for the first train and the measured amplitudes during the x-scan. Only photons reaching the PMT within 250 ps of the first photon hit are included by the simulation.

3.6 A PMT response model

An approximate model for the PMT response was developed in an attempt to explain the prevailing amplitude histogram shape with a long tail. The basic assumption is that the voltage response amplitudes to a single photoelectron have a Gaussian distribution. The number of photons generated in a bar follows the Poisson distribution, so the number of photoelectrons in the PMT does too. The model (Equation 3.1) is then a simple sum over all photoelectron counts, each represented by a Gaussian and weighted by the appropriate Poisson factor:

$$p(u) = \sum_{n=1}^{\infty} \left(\underbrace{\frac{\lambda^n e^{-\lambda}}{n!}}_{\text{Poisson factor}} \underbrace{\frac{1}{\sigma(n)} e^{-\frac{1}{2}\left(\frac{u-n\overline{u}_1}{\sigma(n)}\right)^2}}_{\text{Gaussian}} \right) . \tag{3.1}$$

In the model, $p(u)$ is proportional to the probability of response with an amplitude u occurring (the model is not normalized). The individual Gaussian widths follow $\sigma(n) = \sigma_1\sqrt{n}$, where σ_1 is the width of the single photoelectron Gaussian, $\overline{u}_1$ is it's mean. The λ is the average number of photoelectrons, $\overline{N}_{\text{pe}} = \lambda$.

In a real application of the model it is sufficient to sum only for $n \leq 2.5\lambda + 5$, with higher n the Poisson distribution suppresses the effect of the Gaussians enough to be negligible. An example output of the model is in Figure 3.31.

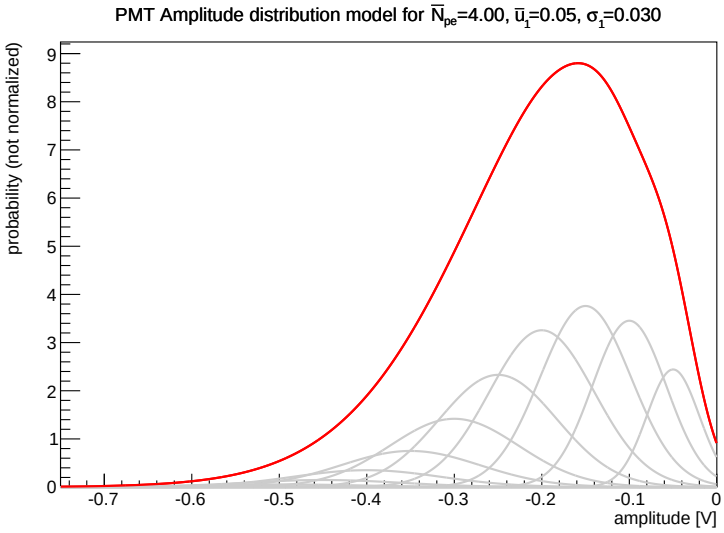

Figure 3.31: An example of the PMT response model. The gray Gaussians sum up to the red distribution.

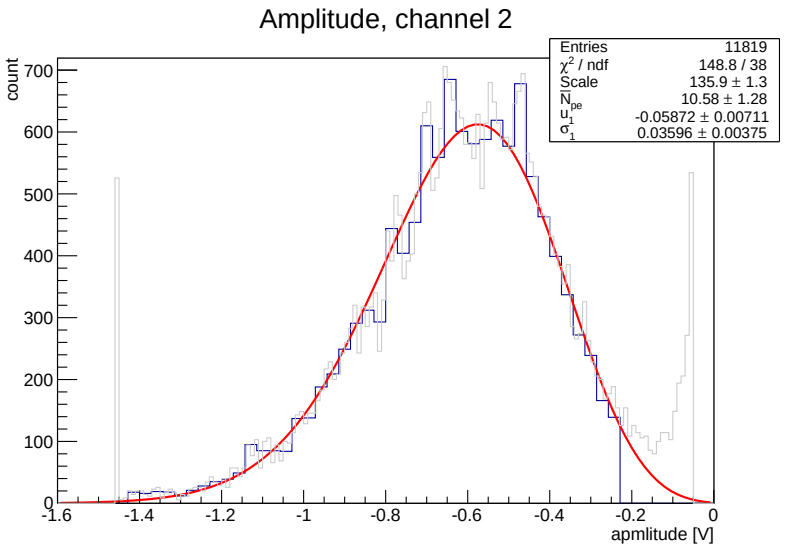

Figure 3.32: The PMT model used to fit a real PMT response amplitude histogram.

The model can be used to fit a real measurement data as in Figure 3.32. The fit $\overline{N}_{\mathrm{pe}}$ is grossly underestimated compared to the simulation, because in the reality the photons are spread over time, while the model expects their effect to simply sum up. The histogram shape is well explained by this model however, suggesting that the general approach is correct.

Summary

This thesis covers the work on simulation and data analysis of the September 2015 AFP Test Beam measurements. The AFP detector is a detector in the forward region of the ATLAS detector at the LHC. The measurements are meant to evaluate the Time-of-Flight (ToF) detector, used to distinguish from which vertex in the interaction point the incoming particle originates. It is designed to operate by measuring the time the particle passes through with very high precision (down to 10 ps).

The ToF detector consists of fused silica bars (four trains of four bars), acting as the active medium generating a Cherenkov radiation, which is then guided towards and detected by a photomultiplier. This signal is then amplified and a precise timing information is determined. A train is a series of bars that get hit by the same particle, in theory providing four independent measurements to increase the resolution by the factor of $\frac{1}{\sqrt{n}}$, where $n = 4$.

Both the simulation and the measurement data analysis focus on the raw signal measurements, where the photomultiplier response is measured by an oscilloscope after being amplified. However, only a subset of the detector design was tested, leaving some of the photomultiplier channels empty.

By performing a visual inspection of the photon tracks in the simulation, the mechanism responsible for the high optical crosstalk was identified. Monte Carlo simulations were then performed, giving a basis for a deeper analysis of the optical crosstalk as well as some other properties of the ToF optical part.

The crosstalk within a train was analysed and a strong dependence on the x position of the particle hitting the detector was observed, with the magnitude of the crosstalk peaking at 4.3 mm from the bar edge. The same edge effect that is helping a bar to gather more photons near the end of the bar is responsible for capturing the photons originating from the previous bars.

This crosstalk however occurs only within a train, where it does not introduce any correlation between the bars. No optical crosstalk is occurring between the neighbouring trains, which is vital for dealing with high pileup situations, when the ToF detector would need to detect hits in multiple trains at once.

A dependence of the measured time on the detector hit position was observed during the x-scan simulation. It is crucial that this is well understood and calibrated for the ToF detector to perform optimally. The effect predicted by the simulation was slightly visible in the x-scan measurement data peak times, but the timing resolution of these measurements was not good enough to allow for a comparison with simulation or for derivation of a precise correction. This will have to be done based on the CFD (Constant Fraction Discriminator) measurements or after installation in the tunnel by comparing with the tracker hits directly during low pileup runs.

The influence of a slightly different design of the first train of bars was studied, yielding a somewhat stronger response. This design cannot be used for all trains,

otherwise the required area would not be covered by the ToF detector. The time distribution of the photon hits was also evaluated for both bar designs.

Analysis of the Test Beam data focused on the amplitude distributions and amplitude correlations, while some other signal parameters were used for the necessary cuts.

The optical crosstalk estimate based on comparing amplitudes for bars within a train was higher than that predicted by the simulation, possible reasons were discussed, such as a physical contact of the bars. The amplitude dependence on the hit position was then studied, giving fairly similar results as the simulation.

Correlations between the bars in a train could negatively influence the $\frac{1}{\sqrt{n}}$ resolution improvement. The analysis showed the amplitude correlations peaking at $\sim 12\,\%$ and proved that the optical crosstalk was not the source of these correlations. Also the correlation, caused mostly by the photomultiplier charge sharing effect, was not present when a one channel gap between the bars was left. No correlation for measurements with a gap means that the correlations worsen the resolution only for the immediate neighbours. Therefore not too much effect on the timing resolution in the complete detector is expected and performance close to the theoretical $\frac{1}{\sqrt{n}}$ improvement could be achieved. This effect will be further reduced by a modified photomultiplier, which would also feature ALD (atomic layer deposition) treatment of microchannel plates, prolonging its lifetime.

A comparison between the signal amplitude and the signal area showed a near perfect correlation. Therefore the photomultiplier response was not changing shape significantly, which could degrade the timing performance.

A dependence of the signal amplitude on the photomultiplier high voltage was observed, behaving as expected.

The effect of an optical grease application between the ends of the bars and the photomultiplier was analysed, proving that the amplitudes increase significantly, while being very sensitive to a correct grease application. However, the timing resolution for these measurements was not improved much, therefore this approach is abandoned for being a possible cause of complications.

The amplitude of the measurements was directly compared to the number of photoelectrons predicted by the simulation. By applying a 250 ps window on the photon arrival times in the simulation, this comparison significantly improved, while still suffering from a lack of a proper photomultiplier model, causing different ratios for the two bars.

Finally, a rough outline of a model of the photomultiplier response was described, providing a plausible explanation for the prevailing amplitude histogram shapes.

Bibliography

[1] ATLAS-AFP Collaboration: *Technical Design Report for the ATLAS Forward Proton Detector*. CERN-LHCC-2015-009; ATLAS-TDR-024-2015.

[2] HAMAL, P.; SYKORA, T.: *Exclusive Pion Production Measured by ATLAS*. WDS'15 Proceedings of Contributed Papers – Physics, MATFYZPRESS 2015.

[3] KOMÁREK, T. *Vizualizace drah částic v magnetickém poli urychlovače.* Bakalářská práce, Univerzita Palckého v Olomouci, Přírodovědecká fakulta. Olomouc (2013). Dostupné online: `https://theses.cz/id/ikzo0d`.

[4] ATLAS Twiki page *BeamSpotPublicResults*, available online at `https://twiki.cern.ch/twiki/bin/view/AtlasPublic/BeamSpotPublicResults`.

[5] ATLAS Collaboration: *Characterization of Interaction-Point Beam Parameters Using the pp Event-Vertex Distribution Reconstructed in the ATLAS Detector at the LHC*.
Available online at `http://cds.cern.ch/record/1277659`.

[6] *Geant4 Physics Reference Manual*. Geant4 10.2 (4 December 2015). Available online at
`http://geant4.web.cern.ch/geant4/UserDocumentation/UsersGuides/PhysicsReferenceManual/fo/PhysicsReferenceManual.pdf`.

[7] PÉREZ, I.: *A study of the polarization of Cherenkov Radiation in Extensive Air Showers of Energy around 1 TeV*. Available online at
`http://www.iexp.uni-hamburg.de/groups/astroparticle/de/archive/hegra/publ_hegra/tesina-icp.ps.gz`.

[8] ALDA, J.: *Encyclopedia of Optical Engineering*. LVOVSKY, A., chapter *Fresnel Equations*. Available online at `http://www.tandfonline.com/doi/abs/10.1081/E-EOE-120009751`.

[9] *miniPLANACON XPM85112 datasheet*. Photonis. Available online at
`https://www.photonis.com/uploads/datasheet/pd/Mini-PLANACON-4x4-datasheet.pdf`.

[10] ATLAS Twiki page *RCE Development Lab*, available online at
`https://twiki.cern.ch/twiki/bin/viewauth/Atlas/RCEDevelopmentLab`.

[11] NOZKA, L. et. al.: *Design of Cherenkov bars for the optical part of the time-of-flight detector in Geant4*. Opt. Express 22, 28984-28996 (2014).

[12] LANGE, J. et. al.: *Beam Tests of an Integrated Prototype of the ATLAS Forward Proton Detector*. ATLAS note preliminary draft.

List of used symbols and acronyms

c	Speed of light
v_{p}	Speed of particle passing through a medium
n	Index of refraction
E	Energy
μ	Permeability of medium
θ	Cherenkov angle
r	Reflectivity
φ	Angle of incidence or refraction
x, y, z	Spatial coordinates
N_{pe}	Number of photoelectrons
u	PMT voltage response
AFP	ATLAS Forward Proton
ToF	Time-of-Flight (detector)
PMT	Photomultiplier
MCP-PMT	Multi-Channel Plate Photomultiplier
SiPM	Silicon photomultiplier
IP	Interaction Point
MC	Monte Carlo (simulation)
RP	Roman Pot
PAa, PAb	Pre-amplifier stages
HV	PMT High voltage
CFD	Constant Fraction Discriminator
HPTDC	High-Performance Time-to-Digital Converter
RCE	Reconfigurable Cluster Elements system
CFG1	LQBar configuration 1
CFG2	LQBar configuration 2

Appendix

Contents of enclosed CD

```
.:
TB_data
TB_sim

./TB_data:
Amplitudes_LOG16.txt
Amplitudes_LOG17.txt
Amplitudes_LOG24.txt
Amplitudes_LOG25.txt
Amplitudes_LOG57.txt
analysisCode
Comparison_LOG24_LOG57
GatherAmplitudes.sh
LOG16
LOG17
LOG24
LOG25
LOG57
md5s.txt
OscChannelComparison

./TB_data/analysisCode:
amplitudecutoff.cxx
amplitudecutoff.h
coparison-edge_train1_uuuu
fits_ch1.pdf
fits_ch2.pdf
fits_ch3.pdf
fits_ch4.pdf
Makefile
PedestalShape.pdf
PMT_AmpModelFit
processAll.sh
processLOG17.sh
processLOG25.sh
processLOG57.sh
rawAnalysisTB
rawAnalysisTB.cxx
rawAnalysisTB.log

./TB_data/analysisCode/coparison-edge_train1_uuuu:
LOG16.log
LOG16.pdf
LOG24.log
LOG24.pdf

./TB_data/analysisCode/PMT_AmpModelFit:
amplitudecutoff.cxx
amplitudecutoff.h
amplitude.dat
crosstalk
crosstalkTB.cxx
Makefile
out.pdf
rawAnalysisTB-PMT_AmpModelFit.log
rawAnalysisTB-PMT_AmpModelFit.pdf
TB_AmpsModelFit_5mm_train1_uuuu_Page8.pdf
tmpCrosstalkTB.pdf

./TB_data/Comparison_LOG24_LOG57:
Amplitudes_24vs57.ods
PDF_tables

./TB_data/Comparison_LOG24_LOG57/PDF_tables:
Amplitudes_24vs57_compensated-crop.pdf
Amplitudes_24vs57_compensated.pdf
Amplitudes_24vs57-crop.pdf
Amplitudes_24vs57.pdf

./TB_data/LOG16:
5mm_train1_AAAA
5mm_train1_BBBB
5mm_train1_uuuu
5mm_train2_AAAA
5mm_train2_AAAA_1900V
5mm_train2_AAAA_LV30.3V
5mm_train2_BBBB
5mm_train2_uuuu
5mm_train3_AAAA
5mm_train3_BBBB
5mm_train3_llll
5mm_train4_AAAA
5mm_train4_BBBB
5mm_train4_llll
edge_train1_AAAA
edge_train1_BBBB
edge_train1_uuuu
edge_train2_AAAA
edge_train2_BBBB
edge_train2_uuuu
edge_train3_AAAA
edge_train3_BBBB
edge_train3_llll
edge_train4_AAAA
edge_train4_BBBB
edge_train4_llll
log16_raw_edge_cfg1_barsA_amp.png
log16_raw_edge_cfg1_barsA_area.png
log16_raw_edge_cfg1_barsA_esl.png
log16_raw_edge_cfg1_barsB_amp.png
log16_raw_edge_cfg1_barsB_area.png
log16_raw_edge_cfg1_barsB_esl.png
log16_raw_edge_cfg1_trains12_amp.png
log16_raw_edge_cfg1_trains12_area.png
log16_raw_edge_cfg1_trains12_esl.png
log16_raw_edge_cfg1_trains34_amp.png
log16_raw_edge_cfg1_trains34_area.png
log16_raw_edge_cfg1_trains34_esl.png
tof100.jpg
tof101.jpg
tof102.jpg
tof103.jpg
tof104.jpg
tof68.jpg
```

```
tof69.jpg
tof70.jpg
tof71.jpg
tof72.jpg
tof73.jpg
tof74.jpg
tof75.jpg
tof76.jpg
tof77.jpg
tof78.jpg
tof79.jpg
tof80.jpg
tof81.jpg
tof82.jpg
tof83.jpg
tof84.jpg
tof85.jpg
tof86.jpg
tof97.jpg
tof98.jpg
tof99.jpg

./TB_data/LOG16/5mm_train1_AAAA:
amplitude.dat
rawAnalysisTB-5mm_train1_AAAA.log
rawAnalysisTB-5mm_train1_AAAA.pdf

./TB_data/LOG16/5mm_train1_BBBB:
amplitude.dat
rawAnalysisTB-5mm_train1_BBBB.log
rawAnalysisTB-5mm_train1_BBBB.pdf

./TB_data/LOG16/5mm_train1_uuuu:
amplitude.dat
pl12_correlation.pdf
rawAnalysisTB-5mm_train1_uuuu.log
rawAnalysisTB-5mm_train1_uuuu.pdf

./TB_data/LOG16/5mm_train2_AAAA:
amplitude.dat
rawAnalysisTB-5mm_train2_AAAA.log
rawAnalysisTB-5mm_train2_AAAA.pdf

./TB_data/LOG16/5mm_train2_AAAA_1900V:
amplitude.dat
rawAnalysisTB-5mm_train2_AAAA_1900V.log
rawAnalysisTB-5mm_train2_AAAA_1900V.pdf

./TB_data/LOG16/5mm_train2_AAAA_LV30.3V:
amplitude.dat
rawAnalysisTB-5mm_train2_AAAA_LV30.3V.log
rawAnalysisTB-5mm_train2_AAAA_LV30.3V.pdf

./TB_data/LOG16/5mm_train2_BBBB:
amplitude.dat
rawAnalysisTB-5mm_train2_BBBB.log
rawAnalysisTB-5mm_train2_BBBB.pdf

./TB_data/LOG16/5mm_train2_uuuu:
amplitude.dat
rawAnalysisTB-5mm_train2_uuuu.log
rawAnalysisTB-5mm_train2_uuuu.pdf

./TB_data/LOG16/5mm_train3_AAAA:
amplitude.dat
rawAnalysisTB-5mm_train3_AAAA.log
rawAnalysisTB-5mm_train3_AAAA.pdf

./TB_data/LOG16/5mm_train3_BBBB:
amplitude.dat
rawAnalysisTB-5mm_train3_BBBB.log
rawAnalysisTB-5mm_train3_BBBB.pdf

./TB_data/LOG16/5mm_train3_llll:
amplitude.dat
rawAnalysisTB-5mm_train3_llll.log
rawAnalysisTB-5mm_train3_llll.pdf

./TB_data/LOG16/5mm_train4_AAAA:
amplitude.dat
rawAnalysisTB-5mm_train4_AAAA.log
rawAnalysisTB-5mm_train4_AAAA.pdf

./TB_data/LOG16/5mm_train4_BBBB:
amplitude.dat
rawAnalysisTB-5mm_train4_BBBB.log
rawAnalysisTB-5mm_train4_BBBB.pdf

./TB_data/LOG16/5mm_train4_llll:
amplitude.dat
rawAnalysisTB-5mm_train4_llll.log
rawAnalysisTB-5mm_train4_llll.pdf

./TB_data/LOG16/edge_train1_AAAA:
amplitude.dat
rawAnalysisTB-edge_train1_AAAA.log
rawAnalysisTB-edge_train1_AAAA.pdf

./TB_data/LOG16/edge_train1_BBBB:
amplitude.dat
rawAnalysisTB-edge_train1_BBBB.log
rawAnalysisTB-edge_train1_BBBB.pdf

./TB_data/LOG16/edge_train1_uuuu:
amplitude.dat
pl12_correlation.pdf
rangesCheck
rawAnalysisTB-edge_train1_uuuu.log
rawAnalysisTB-edge_train1_uuuu.pdf
tretinySlice

./TB_data/LOG16/edge_train1_uuuu/rangesCheck:
a1.pdf
esl1.pdf
pl1.pdf
pt1.pdf
tp1.pdf
vt1.pdf
vy1.pdf

./TB_data/LOG16/edge_train1_uuuu/tretinySlice:

./TB_data/LOG16/edge_train2_AAAA:
amplitude.dat
rawAnalysisTB-edge_train2_AAAA.log
rawAnalysisTB-edge_train2_AAAA.pdf

./TB_data/LOG16/edge_train2_BBBB:
amplitude.dat
rawAnalysisTB-edge_train2_BBBB.log
rawAnalysisTB-edge_train2_BBBB.pdf

./TB_data/LOG16/edge_train2_uuuu:
amplitude.dat
rawAnalysisTB-edge_train2_uuuu.log
rawAnalysisTB-edge_train2_uuuu.pdf

./TB_data/LOG16/edge_train3_AAAA:
amplitude.dat
rawAnalysisTB-edge_train3_AAAA.log
rawAnalysisTB-edge_train3_AAAA.pdf

./TB_data/LOG16/edge_train3_BBBB:
amplitude.dat
rawAnalysisTB-edge_train3_BBBB.log
rawAnalysisTB-edge_train3_BBBB.pdf

./TB_data/LOG16/edge_train3_llll:
amplitude.dat
rawAnalysisTB-edge_train3_llll.log
rawAnalysisTB-edge_train3_llll.pdf

./TB_data/LOG16/edge_train4_AAAA:
amplitude.dat
rawAnalysisTB-edge_train4_AAAA.log
rawAnalysisTB-edge_train4_AAAA.pdf

./TB_data/LOG16/edge_train4_BBBB:
```

```
amplitude.dat
rawAnalysisTB-edge_train4_BBBB.log
rawAnalysisTB-edge_train4_BBBB.pdf

./TB_data/LOG16/edge_train4_llll:
amplitude.dat
rawAnalysisTB-edge_train4_llll.log
rawAnalysisTB-edge_train4_llll.pdf

./TB_data/LOG17:
1mm_train1_uuuu
1mm_train2_uuuu
2mm_train1_uuuu
2mm_train2_uuuu
3mm_train1_uuuu
3mm_train2_uuuu
4mm_train1_uuuu
4mm_train2_uuuu
8mm_train1_uuuu
8mm_train2_uuuu
tof87.jpg
tof88.jpg
tof89.jpg
tof90.jpg
tof91.jpg
tof92.jpg
tof93.jpg
tof94.jpg
tof95.jpg
tof96.jpg

./TB_data/LOG17/1mm_train1_uuuu:
amplitude.dat
rawAnalysisTB-1mm_train1_uuuu.log
rawAnalysisTB-1mm_train1_uuuu.pdf

./TB_data/LOG17/1mm_train2_uuuu:
amplitude.dat
rawAnalysisTB-1mm_train2_uuuu.log
rawAnalysisTB-1mm_train2_uuuu.pdf

./TB_data/LOG17/2mm_train1_uuuu:
amplitude.dat
rawAnalysisTB-2mm_train1_uuuu.log
rawAnalysisTB-2mm_train1_uuuu.pdf

./TB_data/LOG17/2mm_train2_uuuu:
amplitude.dat
rawAnalysisTB-2mm_train2_uuuu.log
rawAnalysisTB-2mm_train2_uuuu.pdf

./TB_data/LOG17/3mm_train1_uuuu:
amplitude.dat
rawAnalysisTB-3mm_train1_uuuu.log
rawAnalysisTB-3mm_train1_uuuu.pdf

./TB_data/LOG17/3mm_train2_uuuu:
amplitude.dat
LINEAR-SCATTER-CUT_processAll-3mm_train2_uuuu.pdf
NO-SCATTER-CUT_processAll-3mm_train2_uuuu.pdf
rawAnalysisTB-3mm_train2_uuuu.log
rawAnalysisTB-3mm_train2_uuuu.pdf

./TB_data/LOG17/4mm_train1_uuuu:
amplitude.dat
rawAnalysisTB-4mm_train1_uuuu.log
rawAnalysisTB-4mm_train1_uuuu.pdf

./TB_data/LOG17/4mm_train2_uuuu:
amplitude.dat
rawAnalysisTB-4mm_train2_uuuu.log
rawAnalysisTB-4mm_train2_uuuu.pdf

./TB_data/LOG17/8mm_train1_uuuu:
amplitude.dat
rawAnalysisTB-8mm_train1_uuuu.log
rawAnalysisTB-8mm_train1_uuuu.pdf

./TB_data/LOG17/8mm_train2_uuuu:
amplitude.dat
rawAnalysisTB-8mm_train2_uuuu.log
rawAnalysisTB-8mm_train2_uuuu.pdf

./TB_data/LOG24:
5mm_train1_uuuu
5mm_train2_uuuu
5mm_train3_llll
5mm_train4_llll
edge1_train1_uuuu
edge1_train2_uuuu
edge1_train3_llll
edge1_train4_llll
edge_train1_uuuu
edge_train2_uuuu
edge_train3_llll
edge_train4_llll
tof137.png
tof138.png
tof139.png
tof140.png
tof141.png
tof142.png
tof143.png
tof144.png
tof145.png
tof146.png
tof147.png
tof148.png

./TB_data/LOG24/5mm_train1_uuuu:
amplitude.dat
pl12_correlation.pdf
rawAnalysisTB-5mm_train1_uuuu.log
rawAnalysisTB-5mm_train1_uuuu.pdf

./TB_data/LOG24/5mm_train2_uuuu:
amplitude.dat
rawAnalysisTB-5mm_train2_uuuu.log
rawAnalysisTB-5mm_train2_uuuu.pdf

./TB_data/LOG24/5mm_train3_llll:
amplitude.dat
CFG2_CF_5mm_train3_llll.pdf
NO-H2-CUT_processAll-5mm_train3_llll.pdf
rawAnalysisTB-5mm_train3_llll.log
rawAnalysisTB-5mm_train3_llll.pdf

./TB_data/LOG24/5mm_train4_llll:
amplitude.dat
rawAnalysisTB-5mm_train4_llll.log
rawAnalysisTB-5mm_train4_llll.pdf

./TB_data/LOG24/edge1_train1_uuuu:
amplitude.dat
rawAnalysisTB-edge1_train1_uuuu.log
rawAnalysisTB-edge1_train1_uuuu.pdf

./TB_data/LOG24/edge1_train2_uuuu:
amplitude.dat
rawAnalysisTB-edge1_train2_uuuu.log
rawAnalysisTB-edge1_train2_uuuu.pdf

./TB_data/LOG24/edge1_train3_llll:
amplitude.dat
rawAnalysisTB-edge1_train3_llll.log
rawAnalysisTB-edge1_train3_llll.pdf

./TB_data/LOG24/edge1_train4_llll:
amplitude.dat
rawAnalysisTB-edge1_train4_llll.log
rawAnalysisTB-edge1_train4_llll.pdf

./TB_data/LOG24/edge_train1_uuuu:
amplitude.dat
CFG2_CF_edge_train1_uuuu.pdf
NO-H2-CUT_processAll-edge_train1_uuuu.pdf
pl12_correlation.pdf
rawAnalysisTB-edge_train1_uuuu.log
```

```
rawAnalysisTB-edge_train1_uuuu_NoCorrCut.pdf
rawAnalysisTB-edge_train1_uuuu.pdf

./TB_data/LOG24/edge_train2_uuuu:
amplitude.dat
rawAnalysisTB-edge_train2_uuuu.log
rawAnalysisTB-edge_train2_uuuu.pdf

./TB_data/LOG24/edge_train3_llll:
amplitude.dat
CFG2_CF_edge_train3_llll.pdf
NO-H2-CUT_processAll-edge_train3_llll.pdf
rawAnalysisTB-edge_train3_llll.log
rawAnalysisTB-edge_train3_llll.pdf

./TB_data/LOG24/edge_train4_llll:
amplitude.dat
rawAnalysisTB-edge_train4_llll.log
rawAnalysisTB-edge_train4_llll.pdf

./TB_data/LOG25:
edge_train2_1850V_uuuu
edge_train2_1870V_uuuu
edge_train2_1900V_uuuu
edge_train2_1930V_uuuu
tof149.png
tof150.png
tof151.png
tof152.png

./TB_data/LOG25/edge_train2_1850V_uuuu:
amplitude.dat
rawAnalysisTB-edge_train2_1850V_uuuu.log
rawAnalysisTB-edge_train2_1850V_uuuu.pdf

./TB_data/LOG25/edge_train2_1870V_uuuu:
amplitude.dat
rawAnalysisTB-edge_train2_1870V_uuuu.log
rawAnalysisTB-edge_train2_1870V_uuuu.pdf

./TB_data/LOG25/edge_train2_1900V_uuuu:
amplitude.dat
rawAnalysisTB-edge_train2_1900V_uuuu.log
rawAnalysisTB-edge_train2_1900V_uuuu.pdf

./TB_data/LOG25/edge_train2_1930V_uuuu:
amplitude.dat
rawAnalysisTB-edge_train2_1930V_uuuu.log
rawAnalysisTB-edge_train2_1930V_uuuu.pdf

./TB_data/LOG57:
5mm_train1_uuuu
5mm_train2_uuuu
5mm_train3_llll
5mm_train4_llll
edge1_train1_uuuu
edge1_train2_uuuu
edge1_train3_llll
edge1_train4_llll
edge_train1_uuuu
edge_train2_uuuu
edge_train3_llll
edge_train4_llll

./TB_data/LOG57/5mm_train1_uuuu:
amplitude.dat
rawAnalysisTB-5mm_train1_uuuu.log
rawAnalysisTB-5mm_train1_uuuu.pdf

./TB_data/LOG57/5mm_train2_uuuu:
amplitude.dat
rawAnalysisTB-5mm_train2_uuuu.log
rawAnalysisTB-5mm_train2_uuuu.pdf

./TB_data/LOG57/5mm_train3_llll:
amplitude.dat
rawAnalysisTB-5mm_train3_llll.log
rawAnalysisTB-5mm_train3_llll.pdf

./TB_data/LOG57/5mm_train4_llll:
amplitude.dat
rawAnalysisTB-5mm_train4_llll.log
rawAnalysisTB-5mm_train4_llll.pdf

./TB_data/LOG57/edge1_train1_uuuu:
amplitude.dat
rawAnalysisTB-edge1_train1_uuuu.log
rawAnalysisTB-edge1_train1_uuuu.pdf

./TB_data/LOG57/edge1_train2_uuuu:
amplitude.dat
rawAnalysisTB-edge1_train2_uuuu.log
rawAnalysisTB-edge1_train2_uuuu.pdf

./TB_data/LOG57/edge1_train3_llll:
amplitude.dat
rawAnalysisTB-edge1_train3_llll.log
rawAnalysisTB-edge1_train3_llll.pdf

./TB_data/LOG57/edge1_train4_llll:
amplitude.dat
rawAnalysisTB-edge1_train4_llll.log
rawAnalysisTB-edge1_train4_llll.pdf

./TB_data/LOG57/edge_train1_uuuu:
amplitude.dat
rawAnalysisTB-edge_train1_uuuu.log
rawAnalysisTB-edge_train1_uuuu.pdf

./TB_data/LOG57/edge_train2_uuuu:
amplitude.dat
rawAnalysisTB-edge_train2_uuuu.log
rawAnalysisTB-edge_train2_uuuu.pdf

./TB_data/LOG57/edge_train3_llll:
amplitude.dat
rawAnalysisTB-edge_train3_llll.log
rawAnalysisTB-edge_train3_llll.pdf

./TB_data/LOG57/edge_train4_llll:
amplitude.dat
rawAnalysisTB-edge_train4_llll.log
rawAnalysisTB-edge_train4_llll.pdf

./TB_data/OscChannelComparison:
AmplitudeFitValues.png
compareList.txt
compareNoAmpList.txt
edge_1A
edge_1B
edge_2A
edge_2B
histo_AorB.root
histo_UorL.root
LOG24NoGrease_Vs_LOG57Grease.txt
overlayPlotGen.C
PDFs
processCompare.sh
rootfiles
tmpHistGen.C
VoltsPerDiv_LOG16.png

./TB_data/OscChannelComparison/edge_1A:
histo_AAAA.root
histo_uuuu.root
uuuu_vs_AAAA_25bins.pdf
uuuu_vs_AAAA_25bins.root
uuuu_vs_AAAA.pdf
uuuu_vs_AAAA.root

./TB_data/OscChannelComparison/edge_1B:
compare.pdf
compare.root
histo_AABB.root
histo_uuuu.root

./TB_data/OscChannelComparison/edge_2A:
comparison.pdf
```

```
comparison.root
histo_AABB.root
histo_uull.root

./TB_data/OscChannelComparison/edge_2B:
comparison.pdf
comparison_rescaledB.pdf
comparison_rescaledB.root
comparison.root
histo_AABB.root
histo_uull.root

./TB_data/OscChannelComparison/PDFs:
diffBars
LOG24NoGrease_Vs_LOG57Grease
sameBars

./TB_data/OscChannelComparison/PDFs/diffBars:
5mmAB_2Avs3A.pdf
5mmAB_2Avs4A.pdf
5mmAB_2Bvs3B.pdf
5mmAB_2Bvs4B.pdf
5mmUL_2Avs3A.pdf
5mmUL_2Avs4A.pdf
5mmUL_2Bvs3B.pdf
5mmUL_2Bvs4B.pdf
edgeAB_2Avs3A.pdf
edgeAB_2Avs4A.pdf
edgeAB_2Bvs3B.pdf
edgeAB_2Bvs4B.pdf
edgeUL_2Avs4A.pdf
edgeUL_2Bvs4B.pdf
edgeUL_3Avs4A.pdf
edgeUL_3Bvs4B.pdf

./TB_data/OscChannelComparison/
/PDFs/LOG24NoGrease_Vs_LOG57Grease:
5mm-1A-No_grease_vs_grease.pdf
5mm-1B-No_grease_vs_grease.pdf
5mm-2A-No_grease_vs_grease.pdf
5mm-2B-No_grease_vs_grease.pdf
5mm-3A-No_grease_vs_grease.pdf
5mm-3B-No_grease_vs_grease.pdf
5mm-4A-No_grease_vs_grease.pdf
5mm-4B-No_grease_vs_grease.pdf
edge1-1A-No_grease_vs_grease.pdf
edge1-1B-No_grease_vs_grease.pdf
edge1-2A-No_grease_vs_grease.pdf
edge1-2B-No_grease_vs_grease.pdf
edge1-3A-No_grease_vs_grease.pdf
edge1-3B-No_grease_vs_grease.pdf
edge1-4A-No_grease_vs_grease.pdf
edge1-4B-No_grease_vs_grease.pdf
edge-1A-No_grease_vs_grease.pdf
edge-1B-No_grease_vs_grease.pdf
edge-2A-No_grease_vs_grease.pdf
edge-2B-No_grease_vs_grease.pdf
edge-3A-No_grease_vs_grease.pdf
edge-3B-No_grease_vs_grease.pdf
edge-4A-No_grease_vs_grease.pdf
edge-4B-No_grease_vs_grease.pdf

./TB_data/OscChannelComparison/PDFs/sameBars:
5mm_1A.pdf
5mm_1B.pdf
5mm_2A.pdf
5mm_2B.pdf
5mm_3A.pdf
5mm_3B.pdf
5mm_4A.pdf
5mm_4B.pdf
edge_1A.pdf
edge_1B.pdf
edge_2A.pdf
edge_2B.pdf
edge_3A.pdf
edge_3B.pdf
edge_4A.pdf
edge_4B.pdf

./TB_data/OscChannelComparison/rootfiles:

./TB_sim:
CrosstalkAnalysis_T1
CrosstalkAnalysis_T2
currentEvent.rndm
currentRun.rndm
g4_00.wrl
g4_01.wrl
g4_02.wrl
g4_03.wrl
g4_04.wrl
g4_05.wrl
g4_06.wrl
g4_07.wrl
g4_08.wrl
g4_09.wrl
g4_10.wrl
g4_11.wrl
scan.mac
vis_t1_0.1mm.mac
vis_t1_5.8mm.mac
vis_t2_0.1mm.mac
vis_t2_5.8mm.mac
xscan_sim

./TB_sim/CrosstalkAnalysis_T1:
_crosstalk_0_1mm.C
crosstalk_0_1mm.C
crosstalk.C
Crosstalk_SideView_T1_0.1mm.png
Crosstalk_SideView_T1_5.8mm.png
Crosstalk_T1_0.1mm.pdf
Crosstalk_T1_5.8mm.pdf

./TB_sim/CrosstalkAnalysis_T2:
crosstalk_0_1mm.C
crosstalk.C
Crosstalk_T2_0.1mm.pdf
Crosstalk_T2_5.8mm.pdf

./TB_sim/xscan_sim:
FirstHitTime
Makefile
scan_0-5mm.log
scan_0-8mm.log
scan_0-8mm.mac
vis_scan_0-5mm.mac
xscan
xscan_0-8mm.cxx
xscan-Sim_0-8mm.log
xscan_TBdata_Sim_comparison.pdf

./TB_sim/xscan_sim/FirstHitTime:
firstHitTime_xscan_labels.png
firstHitTime_xscan.pdf
```